



# TECH BRIEFS

NATIONAL AERONAUTICS AND SPACE ADMINISTRATION

-  **Technology Focus**
-  **Computers/Electronics**
-  **Software**
-  **Materials**
-  **Mechanics**
-  **Machinery/Automation**
-  **Manufacturing**
-  **Bio-Medical**
-  **Physical Sciences**
-  **Information Sciences**
-  **Books and Reports**



## INTRODUCTION

Tech Briefs are short announcements of innovations originating from research and development activities of the National Aeronautics and Space Administration. They emphasize information considered likely to be transferable across industrial, regional, or disciplinary lines and are issued to encourage commercial application.

### Availability of NASA Tech Briefs and TSPs

Requests for individual Tech Briefs or for Technical Support Packages (TSPs) announced herein should be addressed to

#### National Technology Transfer Center

Telephone No. (800) 678-6882 or via World Wide Web at [www2.nttc.edu/leads/](http://www2.nttc.edu/leads/)

Please reference the control numbers appearing at the end of each Tech Brief. Information on NASA's Commercial Technology Team, its documents, and services is also available at the same facility or on the World Wide Web at [www.nctn.hq.nasa.gov](http://www.nctn.hq.nasa.gov).

Commercial Technology Offices and Patent Counsels are located at NASA field centers to provide technology-transfer access to industrial users. Inquiries can be made by contacting NASA field centers and program offices listed below.

## NASA Field Centers and Program Offices

#### Ames Research Center

Carolina Blake  
(650) 604-1754  
[carolina.m.blake@nasa.gov](mailto:carolina.m.blake@nasa.gov)

#### Dryden Flight Research Center

Jenny Baer-Riedhart  
(661) 276-3689  
[jenny.baer-riedhart@dfrc.nasa.gov](mailto:jenny.baer-riedhart@dfrc.nasa.gov)

#### Goddard Space Flight Center

Nona Cheeks  
(301) 286-5810  
[Nona.K.Cheeks.1@gssc.nasa.gov](mailto:Nona.K.Cheeks.1@gssc.nasa.gov)

#### Jet Propulsion Laboratory

Art Murphy, Jr.  
(818) 354-3480  
[arthur.j.murphy-jr@jpl.nasa.gov](mailto:arthur.j.murphy-jr@jpl.nasa.gov)

#### Johnson Space Center

Charlene E. Gilbert  
(281) 483-3809  
[commercialization@jsc.nasa.gov](mailto:commercialization@jsc.nasa.gov)

#### Kennedy Space Center

Jim Aliberti  
(321) 867-6224  
[Jim.Aliberti-1@ksc.nasa.gov](mailto:Jim.Aliberti-1@ksc.nasa.gov)

#### Langley Research Center

Jesse Midgett  
(757) 864-3936  
[jesse.c.midgett@nasa.gov](mailto:jesse.c.midgett@nasa.gov)

#### John H. Glenn Research Center at Lewis Field

Larry Viterna  
(216) 433-3484  
[cto@grc.nasa.gov](mailto:cto@grc.nasa.gov)

#### Marshall Space Flight Center

Vernotto McMillan  
(256) 544-2615  
[vernotto.mcmillan@msfc.nasa.gov](mailto:vernotto.mcmillan@msfc.nasa.gov)

#### Stennis Space Center

Robert Bruce  
(228) 688-1929  
[robert.c.bruce@nasa.gov](mailto:robert.c.bruce@nasa.gov)

#### NASA Program Offices

At NASA Headquarters there are seven major program offices that develop and oversee technology projects of potential interest to industry:

#### Carl Ray

Small Business Innovation Research Program (SBIR) & Small Business Technology Transfer Program (STTR)  
(202) 358-4652 or  
[cray@mail.hq.nasa.gov](mailto:cray@mail.hq.nasa.gov)

#### Benjamin Neumann

Innovative Technology Transfer Partnerships (Code RP)  
(202) 358-2320  
[benjamin.j.neumann@nasa.gov](mailto:benjamin.j.neumann@nasa.gov)

#### John Mankins

Office of Space Flight (Code MP)  
(202) 358-4659 or  
[jmankins@mail.hq.nasa.gov](mailto:jmankins@mail.hq.nasa.gov)

#### Terry Hertz

Office of Aero-Space Technology (Code RS)  
(202) 358-4636 or  
[thertz@mail.hq.nasa.gov](mailto:thertz@mail.hq.nasa.gov)

#### Glen Mucklow

Office of Space Sciences (Code SM)  
(202) 358-2235 or  
[gmucklow@mail.hq.nasa.gov](mailto:gmucklow@mail.hq.nasa.gov)

#### Roger Crouch

Office of Microgravity Science Applications (Code U)  
(202) 358-0689 or  
[rcrouch@hq.nasa.gov](mailto:rcrouch@hq.nasa.gov)

#### Granville Paules

Office of Mission to Planet Earth (Code Y)  
(202) 358-0706 or  
[gpaules@mtpe.hq.nasa.gov](mailto:gpaules@mtpe.hq.nasa.gov)





# TECH BRIEFS

NATIONAL AERONAUTICS AND SPACE ADMINISTRATION



## 5 Technology Focus: Sensors

- 5 Optoelectronic Sensor System for Guidance in Docking
- 6 Hybrid Piezoelectric/Fiber-Optic Sensor Sheets
- 6 Multisensor Arrays for Greater Reliability and Accuracy
- 7 Integrated-Optic Oxygen Sensors
- 8 Ka-Band Autonomous Formation Flying Sensor
- 8 CMOS VLSI Active-Pixel Sensor for Tracking



## 11 Electronics/Computers

- 11 Lightweight, Self-Deploying Foam Antenna Structures
- 11 Electrically Small Microstrip Quarter-Wave Monopole Antennas
- 12 A 2-to-48-MHz Phase-Locked Loop
- 13 Portable Electromyograph



## 15 Software

- 15 Open-Source Software for Modeling of Nanoelectronic Devices
- 15 Software for Generating Strip Maps From SAR Data
- 15 Calibration Software for Use With Jurassicprok
- 15 Software for Probabilistic Risk Reduction
- 16 Software Processes SAR Motion-Measurement Data



## 17 Materials

- 17 Improved Method of Purifying Carbon Nanotubes
- 17 Patterned Growth of Carbon Nanotubes or Nanofibers
- 18 Lightweight, Rack-Mountable Composite Cold Plate/Shelves



## 19 Mechanics

- 19 SiC-Based Miniature High-Temperature Cantilever Anemometer

- 20 Inlet Housing for a Partial-Admission Turbine



## 21 Manufacturing

- 21 Lightweight Thermoformed Structural Components and Optics
- 22 Growing High-Quality InAs Quantum Dots for Infrared Lasers



## 23 Physical Sciences

- 23 Selected Papers on Protoplanetary Disks
- 23 Module for Oxygenating Water Without Generating Bubbles
- 24 Coastal Research Imaging Spectrometer
- 25 Rapid Switching and Modulation by Use of Coupled VCSELS
- 26 Laser-Induced-Fluorescence Photogrammetry and Videogrammetry
- 27 Laboratory Apparatus Generates Dual-Species Cold Atomic Beam
- 27 Laser Ablation of Materials for Propulsion of Spacecraft
- 28 Small Active Radiation Monitor



## 29 Information Sciences

- 29 Hybrid Image-Plane/Stereo Manipulation
- 29 Partitioning a Gridded Rectangle Into Smaller Rectangles
- 30 Digital Radar-Signal Processors Implemented in FPGAs



## 33 Books & Reports

- 33 Part 1 of a Computational Study of a Drop-Laden Mixing Layer
- 33 Some Improvements in Signal-Conditioning Circuits

This document was prepared under the sponsorship of the National Aeronautics and Space Administration. Neither the United States Government nor any person acting on behalf of the United States Government assumes any liability resulting from the use of the information contained in this document, or warrants that such use will be free from privately owned rights.





## Optoelectronic Sensor System for Guidance in Docking

Guidance data are derived from images of illuminated targets.

Marshall Space Flight Center, Alabama

The Video Guidance Sensor (VGS) system is an optoelectronic sensor that provides automated guidance between two vehicles. In the original intended application, the two vehicles would be spacecraft docking together, but the basic principles of design and operation of the sensor are applicable to aircraft, robots, vehicles, or other objects that may be required to be aligned for docking, assembly, resupply, or precise separation.

The system includes a sensor head containing a monochrome charge-coupled-device video camera and pulsed laser diodes mounted on the tracking vehicle, and passive reflective targets on the tracked vehicle. The lasers illuminate the targets, and the resulting video images of the targets are digitized. Then, from the positions of the digitized target images and known geometric relationships among the targets, the relative position and orientation of the vehicles are computed.

As described thus far, the VGS system is based on the same principles as those of the system described in "Improved Video Sensor System for Guidance in Docking" (MFS-31150), *NASA Tech Briefs*, Vol. 21, No. 4 (April 1997), page 9a. However, the two systems differ in the details of design and operation.

The VGS system is designed to operate with the target completely visible within a relative-azimuth range of  $\pm 10.5^\circ$  and a relative-elevation range of  $\pm 8^\circ$ . The VGS acquires and tracks the target within that field of view at any distance from 1.0 to 110 m and at any relative roll, pitch, and/or yaw angle within  $\pm 10^\circ$ . The VGS produces sets of distance and relative-orientation data at a repetition rate of 5 Hz. The software of this system also accommodates the simultaneous operation of two sensors for redundancy.

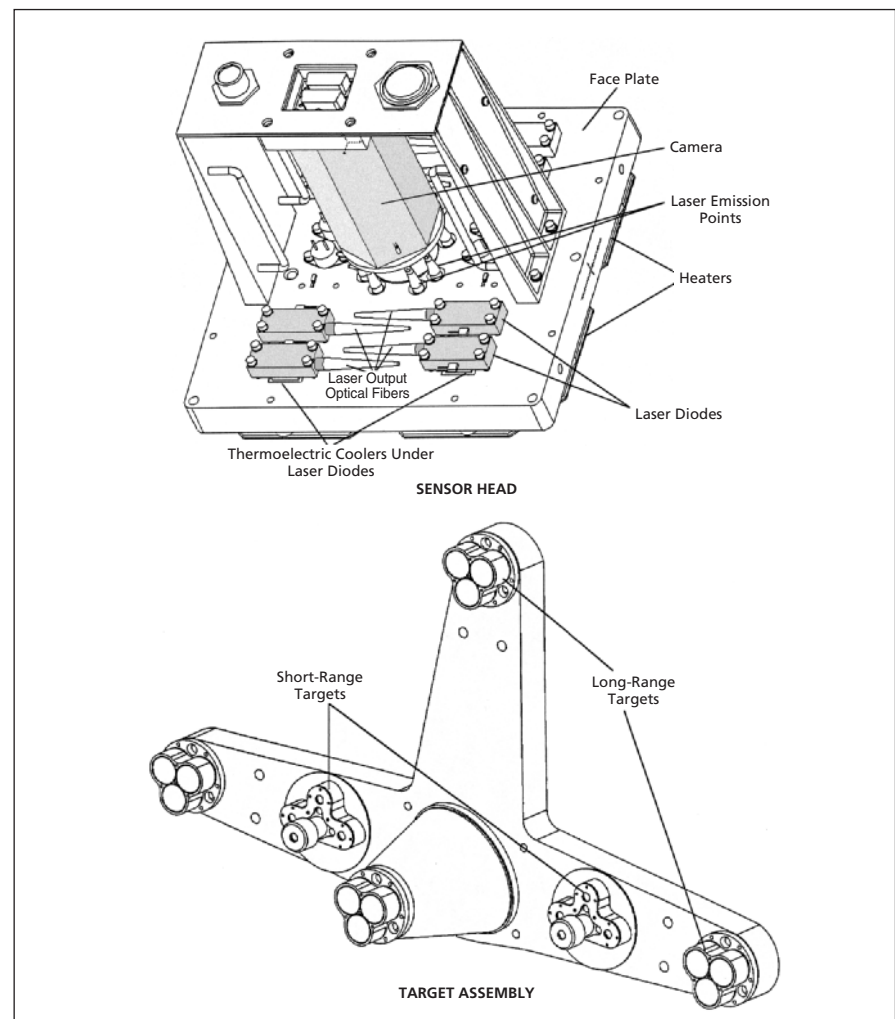
The figure depicts the sensor head and the targets. In addition to the sensor head, the active part of the VGS includes an electronics module. The sensor head must be mounted where it will be aligned with the target when the two vehicles are docked, and the electronics module could be mounted nearby, connected by a set of cables. In addition to the laser

diodes and the video camera, the sensor head contains a sunlight-rejection filter, thermoelectric coolers (to keep the laser-diode temperatures below  $25^\circ\text{C}$ ), heaters (to keep the entire sensor head above  $3^\circ\text{C}$ ), and temperature sensors.

There are eight laser diodes, of which four operate at a wavelength of 800 nm and the other four at 850 nm. The laser outputs are fed through optical fibers to emission points arranged in a circle as close as possible to the video-camera lens. The camera is equipped with an infrared lens and with a double-hump band-pass filter where the humps are 800 and 850-nm.

The electronics module (not shown) contains a power supply, temperature sensors, and five electronic-circuit cards, as follows: (1) a single-board computer, (2) a frame grabber/digital signal processor (DSP) card, (3) a camera-control card, (4) a laser-diode control card, and (5) a control card for the thermoelectric coolers. The frame grabber/digital signal processor card performs most of the work of the system, capturing images and processing the image data to calculate the relative positions and orientations.

The target assembly contains sub-assemblies of long-range and short-range



The **Sensor Head and the Target Assembly** are mounted on two different vehicles. The sensor head generates data to guide the automated docking of the two vehicles. The sensor head and target assembly are positioned so that when docking is complete, they are aligned with each other.

targets, all of which are corner-cube retroreflectors. The targets are covered with filters that pass the 850-nm light and block the 800-nm light. The short-range targets are positioned around, and are smaller than, the long-range targets. The short-range targets are equipped with plano-concave lenses; this is necessary to make these targets visible to the camera over a range of angles at distances <1.5 m.

The operating cycle begins with the firing of the 800-nm lasers and capturing the resulting frame of video data; this frame represents a background image because the target filters block the returns from the targets at the 800-nm wavelength. Then the 850-nm lasers are

fired to capture another frame of video data; this frame represents an image that contains the target spots because target filters allow reflection at the 850-nm wavelength. Because the camera operates at a standard 30-Hz video frame rate, the time between frames is short enough to reduce motion-induced noise to an acceptably low level.

To remove the background (and thereby obtain target-image data alone), the DSP subtracts the first frame of video data from the second, and then subtracts a threshold from the resulting frame. Then the DSP processes the image data to group the illuminated pixels into spots and recognizes the targets by associating

the patterns of spots with the known target patterns. The number of targets and their positions in the assembly are designed so that the relative positions and orientations of the sensor head and the target assembly can be computed by iterative numerical solution of the equations that relate the camera/sensor-head geometry to the positions of the target spots in the video image.

*This work was done by Richard T. Howard, Thomas C. Bryan, and Michael L. Book of Marshall Space Flight Center and John L. Jackson of Micro Craft, Inc. For further information, contact Sammy Nabors, MSFC Commercialization Assistance Lead, at sammy.a.nabors@nasa.gov. MFS-31283*

---

## Hybrid Piezoelectric/Fiber-Optic Sensor Sheets

**Multiple sensors of different types could be installed on or in structures.**

*Marshall Space Flight Center, Alabama*

Hybrid piezoelectric/fiber-optic (HyPFO) sensor sheets are undergoing development. They are intended for use in non-destructive evaluation and long-term monitoring of the integrity of diverse structures, including aerospace, aeronautical, automotive, and large stationary ones. It is anticipated that the further development and subsequent commercialization of the HyPFO sensor systems will lead to economic benefits in the form of increased safety, reduction of life-cycle costs through real-time structural monitoring, increased structural reliability, reduction of maintenance costs, and increased readiness for service.

The concept of a HyPFO sensor sheet is a generalization of the concept of a SMART Layer™, which is a patented device that comprises a thin dielectric film containing an embedded network of distributed piezoelectric actuator/sensors. Such a device can

be mounted on the surface of a metallic structure or embedded inside a composite-material structure during fabrication of the structure. There is has been substantial interest in incorporating sensors other than piezoelectric ones into SMART Layer™ networks: in particular, because of the popularity of the use of fiber-optic sensors for monitoring the “health” of structures in recent years, it was decided to incorporate fiber-optic sensors, giving rise to the concept of HyPFO devices.

The development of HyPFO devices has included the development of novel techniques to incorporate fiber-optic sensors into SMART Layer™ devices, as well as the development of ancillary optoelectronic hardware and software. The advantages expected to be afforded by HyPFO sensor sheets include the following:

- It would not be necessary to install each fiber-optic or piezoelectric sensor indi-

vidually on a structure. Sensors would be embedded in thin, flexible films that could easily be mounted on structures in minimal amounts of installation time.

- Because piezoelectric and fiber-optic transducers exploit different signal-transmission mechanisms, interference between piezoelectric and fiber-optic transducers is expected to be minimal.
- Multiple measurements could be performed. For example, fiber-optic sensors could be used to measure temperatures, piezoelectric transducers could be used to measure concentrations of hydrogen, and sensors of both types could be used to monitor acoustic emissions.

*This work was done by Mark Lin and Xinlin Qing of Acellent Technologies, Inc., for Marshall Space Flight Center. For further information, contact the company at info@acellent.com. MFS-31846*

---

## Multisensor Arrays for Greater Reliability and Accuracy

**Calibrations and replacements are needed less frequently than they are for single sensors.**

*John F. Kennedy Space Center, Florida*

Arrays of multiple, nominally identical sensors with sensor-output-processing electronic hardware and software are being developed in order to obtain accuracy, reliability, and lifetime greater than those of single sensors. The conceptual basis of this development lies in the sta-

tistical behavior of multiple sensors and a multisensor-array (MSA) algorithm that exploits that behavior. In addition, advances in microelectromechanical systems (MEMS) and integrated circuits are exploited. A typical sensor unit according to this concept includes multiple MEMS

sensors and sensor-readout circuitry fabricated together on a single chip and packaged compactly with a microprocessor that performs several functions, including execution of the MSA algorithm.

In the MSA algorithm, the readings from all the sensors in an array at a given



A Compact Unit Containing Eight Pressure Sensors, a microprocessor, and other circuitry generates not only a pressure reading of greater than usual precision, but also an assessment of its own reliability and remaining lifetime.

instant of time are compared and the reliability of each sensor is quantified. This comparison of readings and quantification of reliabilities involves the calculation of the ratio between every sensor reading and every other sensor reading, plus calculation of the sum of all such ratios. Then one output reading for the given instant of time is computed as a weighted average of the readings of all the sensors. In this computation, the weight for each sensor is the aforementioned value used to quantify its reliability.

In an optional variant of the MSA algorithm that can be implemented easily, a running sum of the reliability value for each sensor at previous time steps as well as at the present time step is used as the weight of the sensor in calculating the weighted average at the present time step. In this variant, the weight of a sensor that continually fails gradually decreases, so that eventually, its influence over the

output reading becomes minimal: In effect, the sensor system “learns” which sensors to trust and which not to trust.

The MSA algorithm incorporates a criterion for deciding whether there remain enough sensor readings that approximate each other sufficiently closely to constitute a majority for the purpose of quantifying reliability. This criterion is, simply, that if there do not exist at least three sensors having weights greater than a prescribed minimum acceptable value, then the array as a whole is deemed to have failed.

Monte Carlo simulations of the MSA algorithm on a computational model of a representative multisensor array have demonstrated that a sensor package equipped to implement the MSA algorithm can monitor its own health and estimate its remaining lifetime. In addition, the simulations showed that the array can have a lifetime up to three times that of a single sensor and the er-

rors in the readings delivered by the MSA algorithm are characterized by error bands smaller than those of a single sensor. As a consequential further benefit, calibrations and replacements are needed less frequently than they are in the cases of single sensors.

The figure shows a prototype sensor MSA unit that includes eight surface-mount pressure transducers and an eight-channel multiplexer circuit on a circular circuit board potted with epoxy in a chamber in a sealed aluminum housing. The housing is fitted with a threaded port that gives access to the chamber. A microprocessor and its supporting electronic circuitry are on a separate board that is plugged into the sensor board. The supporting circuitry comprises almost all of the peripheral circuitry needed to complete the functionality of the sensor package, including a self-calibrating 16-bit analog-to-digital converter, a bandgap voltage reference, ample program flash memory, a nonvolatile data memory, and a serial port for communications.

Upon receiving a command to take a measurement, the microprocessor cycles through the multiplexer to measure the voltage from each pressure transducer. It then converts each transducer voltage to a pressure reading via a linear calibration, using unique calibration coefficients for each transducer. The calibration coefficients are stored in the nonvolatile memory and can be easily updated by means of a simple download routine. The pressure readings are entered into the MSA algorithm.

*This work was done by Christopher Immer, Anthony Eckhoff, John Lane, Jose Perotti, John Randazzo, Norman Blalock, and Jeff Rees of Dynacs, Inc. for Kennedy Space Center.*

*This invention is owned by NASA, and a patent application has been filed. Inquiries concerning nonexclusive or exclusive license for its commercial development should be addressed to the Technology Programs and Commercialization Office, Kennedy Space Center, (321) 867-8130. Refer to KSC-12221/359.*

## Integrated-Optic Oxygen Sensors

*Lyndon B. Johnson Space Center, Houston, Texas*

Compact optical oxygen sensors with self-calibration capabilities are undergoing development. A sensor of this type features a single-chip, integrated-optic design implemented by photolithographic fabrication of optical wave-

guides in a photosensitive porous glass. The porosity serves as both a matrix for retention of an oxygen-sensitive fluorescent indicator chemical and a medium for diffusion of oxygen to the chemical from the ambient air to be monitored.

Each sensor includes at least one such waveguide exposed to the atmosphere and at least one covered with metal for isolation from the atmosphere. The covered one serves as a reference channel. In operation, the concentration of oxy-

gen is deduced from the intensity and lifetime of the fluorescence in the exposed channel, with the help of calibration data acquired via the reference channel. Because the sensory chemical is placed directly in and throughout the cross section of the light path, approximately 99 percent of the light in the

waveguide is available for interaction with the chemical, in contradistinction to only about 1 percent of the light in an optical sensor that utilizes evanescent-wave coupling. Hence, a sensor of this type is significantly more sensitive.

*This work was done by Edgar A. Mendoza and Robert A. Lieberman of Physical Optics*

*Corp. and Intelligent Optical Systems, Inc. for Johnson Space Center. For further information, contact:*

*Physical Optics Corp.*

*20600 Gramery Place, Building 100*

*Torrance CA 90501-1821*

*Telephone No.: (310) 320-3088; www.poc.com.*

*Refer to MSC-23085.*

## Ka-Band Autonomous Formation Flying Sensor

*NASA's Jet Propulsion Laboratory, Pasadena, California*

A Ka-band integrated range and bearing-angle formation sensor called the Autonomous Formation Flying (AFF) Sensor has been developed to enable deep-space formation flying of multiple spacecraft. The AFF Sensor concept is similar to that of the Global Positioning System (GPS), but the AFF Sensor would not use the GPS. The AFF Sensor would reside in radio transceivers and signal-processing subsystems aboard the formation-flying spacecraft. A version of the AFF Sensor has been developed for initial application to the two-spacecraft StarLight op-

tical-interferometry mission, and several design investigations have been performed. From the prototype development, it has been concluded that the AFF Sensor can be expected to measure distances and directions with standard deviations of 2 cm and 1 arc minute, respectively, for spacecraft separations ranging up to about 1 km. It has also been concluded that it is necessary to optimize performance of the overall mission through design trade-offs among the performance of the AFF Sensor, the field of view of the AFF Sensor, the designs of the space-

craft and the scientific instruments that they will carry, the spacecraft maneuvers required for formation flying, and the design of a formation-control system.

*This work was done by Jeffrey Tien; George Purcell, Jr.; Jeffrey Srinivasan; Michael Ciminera; Meera Srinivasan; Thomas Meehan; Lawrence Young; MiMi Aung; Luis Amaro; Yong Chong; and Kevin Quirk of Caltech for NASA's Jet Propulsion Laboratory and Dean Paschen of Ball Aerospace Technology Corporation. Further information is contained in a TSP (see page 1). NPO-30813.*

## CMOS VLSI Active-Pixel Sensor for Tracking

**Data could be acquired from as many as eight windows within a frame.**

*NASA's Jet Propulsion Laboratory, Pasadena, California*

An architecture for a proposed active-pixel sensor (APS) and a design to implement the architecture in a complementary metal oxide semiconductor (CMOS) very-large-scale integrated (VLSI) circuit provide for some advanced features that are expected to be especially desirable for tracking point-like features of stars. The architecture would also make this APS suitable for robotic-vision and general pointing and tracking applications.

CMOS imagers in general are well suited for pointing and tracking because they can be configured for random access to selected pixels and to provide readout from windows of interest within their fields of view. However, until now, the architectures of CMOS imagers have not supported multiwindow operation or low-noise data collection. Moreover, smearing and motion artifacts in collected images have made prior CMOS imagers unsuitable for tracking applications.

The proposed CMOS imager (see figure) would include an array of 1,024 by 1,024 pixels containing high-performance photodiode-based APS circuitry. The pixel pitch would be 9  $\mu\text{m}$ . The operations of the pixel circuits would be sequenced and otherwise controlled by an on-chip timing and control block, which would enable the collection of image data, during a single frame period, from either the full frame (that is, all 1,024  $\times$  1,024 pixels) or from within as many as 8 different arbitrarily placed windows as large as 8 by 8 pixels each.

A typical prior CMOS APS operates in a row-at-a-time ("rolling-shutter") readout mode, which gives rise to exposure skew. In contrast, the proposed APS would operate in a sample-first/read-later mode, suppressing rolling-shutter effects. In this mode, the analog readout signals from the pixels corresponding to the windows of the interest (which windows, in the star-tracking application, would presumably contain guide stars)

would be sampled rapidly by routing them through a programmable diagonal switch array to an on-chip parallel analog memory array. The diagonal-switch and memory addresses would be generated by the on-chip controller.

The memory array would be large enough to hold differential signals acquired from all 8 windows during a frame period. Following the rapid sampling from all the windows, the contents of the memory array would be read out sequentially by use of a capacitive transimpedance amplifier (CTIA) at a maximum data rate of 10 MHz. This data rate is compatible with an update rate of almost 10 Hz, even in full-frame operation.

In the multiwindow readout mode, this APS could operate with ultralow noise. When an APS of prior design is operated in row-at-a-time readout, the main component of noise in each pixel is the reset noise at the sensing node. In the proposed APS, the reset levels for an

entire frame would be stored in the memory array, and subsequently used as references during differential readout; that is, for each pixel, its own reset level would be subtracted from its signal. In

other words, this APS would perform on-chip correlated double sampling, eliminating sensing-node reset noise. Hence, the remaining main component of readout noise from each pixel would be that

associated with sampling of the signal and reset levels into the memory array. It has been estimated that using a sampling capacitance of 2 pF (corresponding to a root-mean-square differential sampling noise of  $\approx 65 \mu\text{V}$ ) and a nominal pixel conversion gain of 15  $\mu\text{V}$  per electron, the readout noise would be less than 5 electrons. In full-frame operation, the APS imager would revert to the row-at-a-time readout mode, with a consequent increase in readout noise to 30 electrons.

*This work was done by Bedabrata Pain, Chao Sun, Guang Yang, and Julie Heynssens of Caltech for NASA's Jet Propulsion Laboratory. Further information is contained in a TSP (see page 1).*

*In accordance with Public Law 96-517, the contractor has elected to retain title to this invention. Inquiries concerning rights for its commercial use should be addressed to:*

*Innovative Technology Assets Management:*

*JPL*

*Mail Stop 202-233*

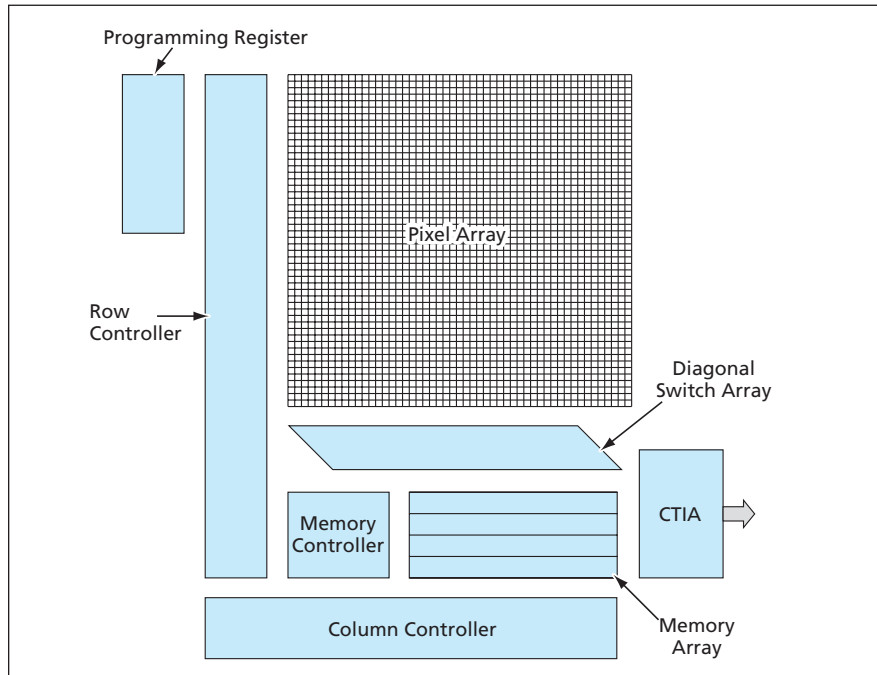
*4800 Oak Grove Drive*

*Pasadena, CA 91109-8099*

*(818) 354-2240*

*E-mail: iaoffice@jpl.nasa.gov*

*Refer to NPO-30440, volume and number of this NASA Tech Briefs issue, and the page number.*



The Proposed CMOS VLSI APS would incorporate on-chip timing and control circuits that would enable operation in either full-frame mode or a programmable multiwindow mode. The multiwindow mode would offer the additional advantage of ultralow noise.





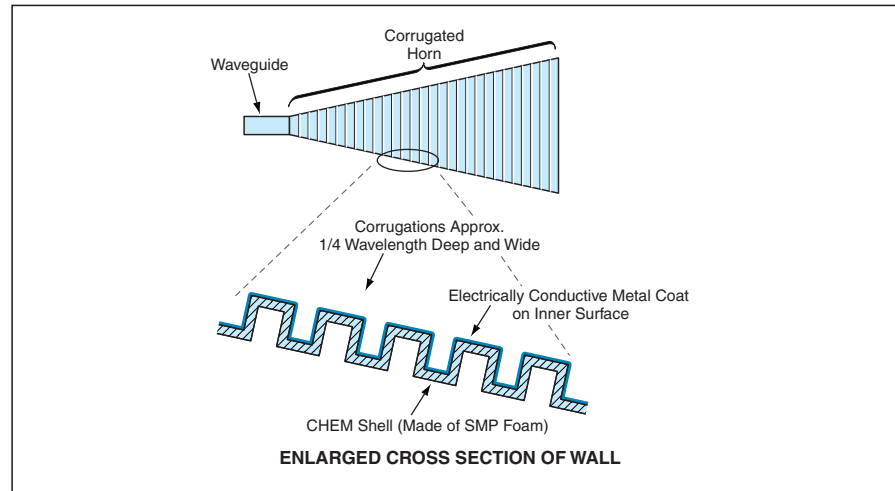
## Lightweight, Self-Deploying Foam Antenna Structures

Advantages would include lightness, simplicity, reliability, compactness in stowage, and low cost.

NASA's Jet Propulsion Laboratory, Pasadena, California

Lightweight, deployable antennas for a variety of outer-space and terrestrial applications would be designed and fabricated according to the concept of cold hibernated elastic memory (CHEM) structures, according to a proposal. Mechanically deployable antennas now in use are heavy, complex, and unreliable, and they utilize packaging volume inefficiently. The proposed CHEM antenna structures would be simple and would deploy themselves without need for any mechanisms and, therefore, would be more reliable. The proposed CHEM antenna structures would also weigh less, could be packaged in smaller volumes, and would cost less, relative to mechanically deployable antennas.

The CHEM concept was described in two prior NASA Tech Briefs articles: "Cold Hibernated Elastic Memory (CHEM) Expandable Structures" (NPO-20394), Vol. 23, No. 2 (February 1999), page 56; and "Solar Heating for Deployment of Foam Structures" (NPO-20961), Vol. 25, No. 10 (October 2001), page 36. To recapitulate from the cited prior articles: The CHEM concept is one of utilizing open-cell foams of shape-memory polymers (SMPs) to make lightweight, reliable, simple, and inexpensive structures that can be alternately (1) compressed and stowed compactly or (2) expanded, then rigidified for use. A CHEM structure is fabricated at full size from a block of SMP foam in its glassy state [at a temperature below the glass-transition temperature ( $T_g$ ) of the SMP]. The structure is heated to the rubbery state of the SMP (that is, to



A CHEM Corrugated Horn Antenna would consist of a lightweight CHEM shell coated with metal on its inner surface.

a temperature above  $T_g$ ) and compacted to a small volume. After compaction, the structure is cooled to the glassy state of the SMP. The compacting force can then be released and the structure remains compact as long as the temperature is kept below  $T_g$ . Upon subsequent heating of the structure above  $T_g$ , the simultaneous elastic recovery of the foam and its shape-memory effect cause the structure to expand to its original size and shape. Once thus deployed, the structure can be rigidified by cooling below  $T_g$ . Once deployed and rigidified, the structure could be heated and recompact. In principle, there should be no limit on the achievable number of compaction/deployment/rigidification cycles.

Thus far, several different designs of a 3.5-m-long CHEM conical corrugated horn antenna have been analyzed (see figure). A small CHEM structural antenna model was fabricated and a thin, electrically conductive layer of aluminum was deposited on the inner surface of the model. This structural model was then subjected to the compaction and deployment treatments described above to demonstrate the feasibility of a CHEM corrugated horn antenna.

*This work was done by Witold Sokolowski, Steven Levin, and Peter Rand of Innovative Technology for NASA's Jet Propulsion Laboratory. Further information is contained in a TSP (see page 1). NPO-30272*

## Electrically Small Microstrip Quarter-Wave Monopole Antennas

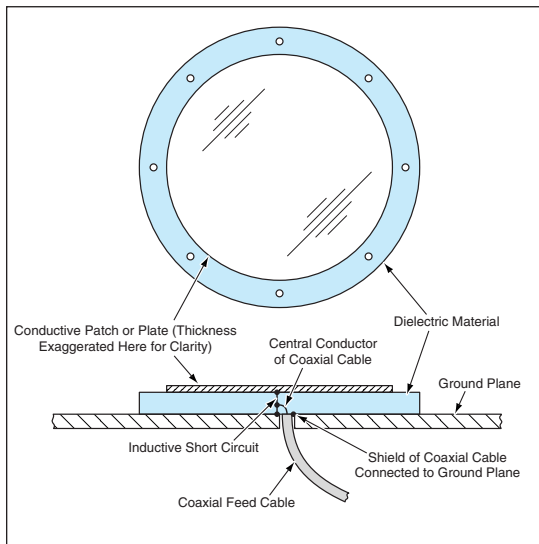
Inductive/resonant feeds make it possible to reduce sizes.

Langley Research Center, Hampton, Virginia

Microstrip-patch-style antennas that generate monopole radiation patterns similar to those of quarter-wave whip antennas can be designed to have dimensions smaller than those needed heretofore for this purpose, by taking advantage

of a feed configuration different from the conventional one. The large sizes necessitated by the conventional feed configuration have, until now, made such antennas impractical for frequencies below about 800 MHz: for example, at 200 MHz, the

conventional feed configuration necessitates a patch diameter of about 8 ft ( $\approx 2.4$  m) — too large, for example, for mounting on the roof of an automobile or on a small or medium-size aircraft. By making it possible to reduce diameters to between



The **Inductive-Short-Circuit Feed Configuration** of this microstrip-style antenna makes it possible for the antenna to have a smaller diameter and still radiate efficiently.

a tenth and a third of that necessitated by the conventional feed configuration, the modified configuration makes it possible to install such antennas in places where they could not previously be installed and thereby helps to realize the potential advantages (concealment and/or reduction of aerodynamic drag) of microstrip versus whip antennas.

In both the conventional approach and the innovative approach, a microstrip-patch (or microstrip-patch-style) antenna for generating a mono-

pole radiation pattern includes an electrically conductive patch or plate separated from an electrically conductive ground plane by a layer of electrically insulating material. In the conventional approach, the electrically insulating layer is typically a printed-circuit board about 1/16 in. ( $\approx 1.6$  mm) thick. Ordinarily, a coaxial cable from a transmitter, receiver, or transceiver is attached at the center on the ground-plane side, the shield of the cable being electrically connected to the ground plane. In the conventional approach, the coaxial cable is mated with a connector mounted on the ground plane. The center pin of this connector connects to the center of the coaxial cable and passes through a hole in the ground plane and a small hole in the insulating layer and then connects with the patch above one-third of the radial distance from the center.

The modified feed configuration of the innovative approach is an inductive-short-circuit configuration that provides impedance matching and that has been used for many years on other antennas but not on microstrip-style monopole antennas. In this configuration, the pin

is connected to both the conductive patch and the ground plane. As before, the shield of the coaxial cable is connected to the ground plane, but now the central conductor is connected to a point on the pin between the ground plane and the conductive plate (see figure). The location of the connection point on the pin is chosen so that together, the inductive short circuit and the conductive plate or patch act as components of a lumped-element resonant circuit that radiates efficiently at the resonance frequency and, at the resonance frequency, has an impedance that matches that of the coaxial cable.

It should be noted that the innovative design entails two significant disadvantages. One disadvantage is that the frequency bandwidth for efficient operation is only about 1/20 to 1/15 that of a whip antenna designed for the same nominal frequency. The other disadvantage is that the estimated gain is between 3-1/2 and 4-1/2 dB below that of the whip antenna. However, if an affected radio-communication system used only a few adjacent frequency channels and the design of the components of the system other than the antenna provided adequate power or gain margin, then these disadvantages could be overcome.

*This work was done by W. Robert Young of Langley Research Center. Further information is contained in a TSP (see page 1). LAR-16330*

## A 2-to-48-MHz Phase-Locked Loop

Noisy and degraded reference clock signals are taken as input and phase-locked clock signals of the same frequency are output with a corrected wave shape.

*Lyndon B. Johnson Space Center, Houston, Texas*

A 2-to-48-MHz phase-locked loop (PLL), developed for the U.S. space program, meets or exceeds all space shuttle clock electrical interface requirements by taking as its reference a 2-to-48-MHz clock signal and outputting a phase-locked clock signal set at the same frequency as the reference clock with transistor-transistor logic (TTL) voltage levels. Because it is more adaptable than other PLLs, the new PLL can be used in industries that employ signaling devices and as a tool in future space missions.

A conventional PLL consists of a phase/frequency detector, loop filter, and voltage-controlled oscillator in which each component exists individually and is integrated into a single de-

vice. PLL components phase-lock to a single frequency or to a narrow bandwidth of frequencies. It is this design, however, that prohibits them from maintaining phase lock to a dynamically changing reference clock when a large bandwidth is required — a deficiency the new PLL overcomes. Since most PLL components require their voltage-controlled oscillators to operate at greater than 2-MHz frequencies, conventional PLLs often cannot achieve the low-frequency phase lock allowed by the new PLL.

The 2-to-48-MHz PLL is built on a wire-wrap board with pins wired to three position jumpers; this makes changing configurations easy. It responds to varia-

tions in voltage-controlled oscillator (VCO) ranges, duty cycle, signal-to-noise ratio (SNR), amplitude, and jitter, exceeding design specifications. A consensus state machine, implemented in a VCO range detector which assures the PLL continues to operate in the correct range, is the primary control state machine for the 2-to-48-MHz PLL circuit. By using seven overlapping frequency ranges with hysteresis, the PLL output sets the resulting phase-locked clock signal at a frequency that agrees with the reference clock with TTL voltage levels.

As a space-shuttle tool, the new PLL circuit takes the noisy, degraded reference clock signals as input and outputs phase-locked clock signals of the same

frequency but with a corrected wave shape. Since its configuration circuit can be easily changed, the new PLL can do the following: readily respond to variations in VCO ranges, duty cycle, SNR, amplitude, and jitter; continuously operate in the correct VCO range because of its consensus state machine; and use its range detector implements

to overlap seven frequency ranges with hysteresis, thus giving the current design a flexibility that exceeds anything available at the time of this development. These features will benefit any industry in which safe and timely clock signals are vital to operation.

*This work was done by Robert D. Koudelka of the Johnson Space Center.*

*This invention is owned by NASA, and a patent application has been filed. Inquiries concerning nonexclusive or exclusive license for its commercial development should be addressed to the Patent Counsel, Johnson Space Center, (281) 483-0837. Refer to MSC-22875.*

## Portable Electromyograph

**Signals from 16 differential EMG electrodes can be recorded for 8 hours.**

*Lyndon B. Johnson Space Center, Houston, Texas*

A portable electronic apparatus records electromyographic (EMG) signals in as many as 16 channels at a sampling rate of 1,024 Hz in each channel. The apparatus (see figure) includes 16 differential EMG electrodes (each electrode corresponding to one channel) with cables and attachment hardware, reference electrodes, an input/output-and-power-adaptor unit, a 16-bit analog-to-digital converter, and a hand-held computer that contains a removable 256-MB flash memory card. When all 16 EMG electrodes are in use, full-bandwidth data can be recorded in each channel for as long as 8 hours. The apparatus is powered by a battery and is small enough that it can be carried in a waist pouch.

The computer is equipped with a small screen that can be used to display the incoming signals on each channel. Amplitude and time adjustments of this display can be made easily by use of touch buttons on the screen. The user can also set up a data-acquisition schedule to conform to experimental proto-



This **Portable Electromyograph** can record signals from as many as 16 differential EMG electrodes. The overall mass of the equipment is 1.1 kg. A wireless version of this device is scheduled for release in the near future.

cols or to manage battery energy and memory efficiently.

Once the EMG data have been recorded, the flash memory card is removed from the EMG apparatus and placed in a flash-memory-card-reading external drive unit connected to a personal computer (PC). The PC can then read the data recorded in the 16 channels. Preferably, before further analysis, the data should be stored in the

hard drive of the PC. The data files are opened and viewed on the PC by use of special-purpose software.

The software for operation of the apparatus resides in a random-access memory (RAM), with backup power supplied by a small internal lithium cell. A backup copy of this software resides on the flash memory card. In the event of loss of both main and backup battery power and consequent loss of this software, the backup copy can be used to restore the RAM copy after power has been restored.

Accessories for this device are also available. These include goniometers, accelerometers, foot switches, and force gauges.

*This work was done by Gianluca De Luca, Carlo J. De Luca, and Per Bergman of DelSys, Inc., for Johnson Space Center. For further information, contact:*

*DelSys Incorporated  
650 Beacon St., 6th floor  
Boston, MA 02215  
Phone: (617) 236-0599  
E-mail: [delsys@delsys.com](mailto:delsys@delsys.com)  
Refer to MSC-23312.*



### Open-Source Software for Modeling of Nanoelectronic Devices

The Nanoelectronic Modeling 3-D (NEMO 3-D) computer program has been upgraded to open-source status through elimination of license-restricted components. The present version functions equivalently to the version reported in “Software for Numerical Modeling of Nanoelectronic Devices” (NPO-30520), *NASA Tech Briefs*, Vol. 27, No. 11 (November 2003), page 37. To recapitulate: NEMO 3-D performs numerical modeling of the electronic transport and structural properties of a semiconductor device that has overall dimensions of the order of tens of nanometers. The underlying mathematical model represents the quantum-mechanical behavior of the device resolved to the atomistic level of granularity. NEMO 3-D solves the applicable quantum matrix equation on a Beowulf-class cluster computer by use of a parallel-processing matrix-vector multiplication algorithm coupled to a Lanczos and/or Rayleigh-Ritz algorithm that solves for eigenvalues. A prior upgrade of NEMO 3-D incorporated a capability for a strain treatment, parameterized for bulk material properties of GaAs and InAs, for two tight-binding submodels. NEMO 3-D has been demonstrated in atomistic analyses of effects of disorder in alloys and, in particular, in bulk  $\text{In}_x\text{Ga}_{1-x}\text{As}$  and in  $\text{In}_{0.6}\text{Ga}_{0.4}\text{As}$  quantum dots.

*This program was written by Fabiano Oyafuso, Hook Hua, Edwin Tisdale, and Gerhard Klimeck of Caltech for NASA’s Jet Propulsion Laboratory. Further information is contained in a TSP (see page 1).*

*This software is available for commercial licensing. Please contact Don Hart of the California Institute of Technology at (818) 393-3425. Refer to NPO-30843.*

### Software for Generating Strip Maps From SAR Data

Jurassicprok is a computer program that generates strip-map digital elevation models and other data products from raw data acquired by an airborne synthetic-aperture radar (SAR) system. This software can process data from a variety of airborne SAR systems but is designed especially for the GeoSAR sys-

tem, which is a dual-frequency (P- and X-band), single-pass interferometric SAR system for measuring elevation both at the bare ground surface and top of the vegetation canopy. Jurassicprok is a modified version of software developed previously for airborne-interferometric-SAR applications. The modifications were made to accommodate P-band interferometric processing, remove approximations that are not generally valid, and reduce processor-induced mapping errors to the centimeter level. Major additions and other improvements over the prior software include the following:

- A new, highly efficient multi-stage-modified wave-domain processing algorithm for accurately motion compensating ultra-wideband data;
- Adaptive regridding algorithms based on estimated noise and actual measured topography to reduce noise while maintaining spatial resolution;
- Exact expressions for height determination from interferogram data;
- Fully calibrated volumetric correlation data based on rigorous removal of geometric and signal-to-noise decorrelation terms;
- Strip range-Doppler image output in user-specified Doppler coordinates;
- An improved phase-unwrapping and absolute-phase-determination algorithm;
- A more flexible user interface with many additional processing options;
- Increased interferogram filtering options; and
- Ability to use disk space instead of random-access memory for some processing steps.

*This program was written by Scott Hensley, Thierry Michel, Soren Madsen, Elaine Chapin, and Ernesto Rodriguez of Caltech for NASA’s Jet Propulsion Laboratory. Further information is contained in a TSP (see page 1).*

*This software is available for commercial licensing. Please contact Don Hart of the California Institute of Technology at (818) 393-3425. Refer to NPO-40032.*

### Calibration Software for Use With Jurassicprok

The Jurassicprok Interferometric Calibration Software (also called “Calibration Processor” or simply “CP”) esti-

mates the calibration parameters of an airborne synthetic-aperture-radar (SAR) system, the raw measurement data of which are processed by the Jurassicprok software described in the preceding article. Calibration parameters estimated by CP include time delays, baseline offsets, phase screens, and radiometric offsets. CP examines raw radar-pulse data, single-look complex image data, and digital elevation map data. For each type of data, CP compares the actual values with values expected on the basis of ground-truth data. CP then converts the differences between the actual and expected values into updates for the calibration parameters in an interferometric calibration file (ICF) and a radiometric calibration file (RCF) for the particular SAR system. The updated ICF and RCF are used as inputs to both Jurassicprok and to the companion Motion Measurement Processor software (described in the following article) for use in generating calibrated digital elevation maps.

*This program was written by Elaine Chapin, Scott Hensley, and Paul Siqueira of Caltech for NASA’s Jet Propulsion Laboratory. Further information is contained in a TSP (see page 1).*

*This software is available for commercial licensing. Please contact Don Hart of the California Institute of Technology at (818) 393-3425. Refer to NPO-40015.*

### Software for Probabilistic Risk Reduction

A computer program implements a methodology, denoted probabilistic risk reduction, that is intended to aid in planning the development of complex software and/or hardware systems. This methodology integrates two complementary prior methodologies: (1) that of probabilistic risk assessment and (2) a risk-based planning methodology, implemented in a prior computer program known as Defect Detection and Prevention (DDP), in which multiple requirements and the beneficial effects of risk-mitigation actions are taken into account. The present methodology and the software are able to accommodate both process knowledge (notably of the efficacy of development practices) and product knowledge (notably of the logical structure of a system, the development of which

one seeks to plan). Estimates of the costs and benefits of a planned development can be derived. Functional and non-functional aspects of software can be taken into account, and trades made among them. It becomes possible to optimize the planning process in the sense that it becomes possible to select the best suite of process steps and design choices to maximize the expectation of success while remaining within budget.

*This program was written by Martin Feather, Steven Cornford, and Leila Meshkat of Caltech and James Kiper of Miami University for NASA's Jet Propulsion Laboratory. Further information is contained in a TSP (see page 1).*

*This software is available for commercial licensing. Please contact Don Hart of the California Institute of Technology at (818) 393-3425. Refer to NPO-40226.*



## Software Processes SAR Motion-Measurement Data

Motion Measurement Processor (MMP) is one of three computer programs that are used together in the operation of a terrain-mapping dual-frequency interferometric synthetic-aperture-radar (SAR) system. The other two programs — Jurassicprok and Calibration Processor — are described in the two immediately preceding articles. MMP acquires all the motion and attitude data collected by onboard instrumentation systems, including radar, laser and camera metrology, inertial navigation systems, and Global Positioning System (GPS) receivers. MMP combines all this information and processes it into all the trajectory information needed to run Jurassicprok, which performs the interferometric processing and mapping functions. MMP includes several Kalman filters for combining and

smoothing aircraft motion and attitude data, and least-squares inversion and filtering software tools for solving for interferometric baseline lengths. MMP synchronizes the motion and radar data. It combines the various measurement data into a unified, seven-dimensional reference system and puts out the resulting filtered trajectory and attitude data along with instructions for use of the data by Jurassicprok, as well as the command files used to operate Jurassicprok.

*This program was written by Adam Freedman, Scott Hensley, Peter Kroger, and Charles T. C. Le of Caltech for NASA's Jet Propulsion Laboratory. Further information is contained in a TSP (see page 1).*

*This software is available for commercial licensing. Please contact Don Hart of the California Institute of Technology at (818) 393-3425. Refer to NPO-40020.*



## Improved Method of Purifying Carbon Nanotubes

Unwanted material is removed without damaging the nanotubes.

Ames Research Center, Moffett Field, California

An improved method of removing the residues of fabrication from carbon nanotubes has been invented. These residues comprise amorphous carbon and metal particles that are produced during the growth process. Prior methods of removing the residues include a variety of processes that involved the use of halogens, oxygen, or air in both thermal and plasma processes. Each of the prior methods entails one or more disadvantages, including non-selectivity (removal or damage of nanotubes in addition to removal of the residues), the need to dispose of toxic wastes, and/or processing times as long as 24 hours or

more. In contrast, the process described here does not include the use of toxic chemicals, the generation of toxic wastes, causes little or no damage to the carbon nanotubes, and involves processing times of less than 1 hour.

In the improved method, purification is accomplished by flowing water vapor through the reaction chamber at elevated temperatures and ambient pressures. The impurities are converted to gaseous waste products by the selective hydrogenation and hydroxylation by the water in a reaction chamber. This process could be performed either immediately after growth or in a post-

growth purification process. The water used needs to be substantially free of oxygen and can be obtained by a repeated freeze-pump-thaw process. The presence of oxygen will non-selectively attach the carbon nanotubes in addition to the amorphous carbon.

*This work was done by Lance D. Delzeit of Ames Research Center and Clement Delzeit. Further information is contained in a TSP (see page 1).*

*Inquiries concerning rights for the commercial use of this invention should be addressed to the Patent Counsel, Ames Research Center, (650) 604-5104. Refer to ARC-14733.*

## Patterned Growth of Carbon Nanotubes or Nanofibers

Numerous parameters of deposition conditions, structures, and compositions affect what is grown.

Ames Research Center, Moffett Field, California

A method and apparatus for the growth of carbon nanotubes or nanofibers in a desired pattern has been invented. The essence of the method is to grow the nanotubes or nanofibers by chemical vapor deposition (CVD) onto a patterned catalyst supported by a substrate.

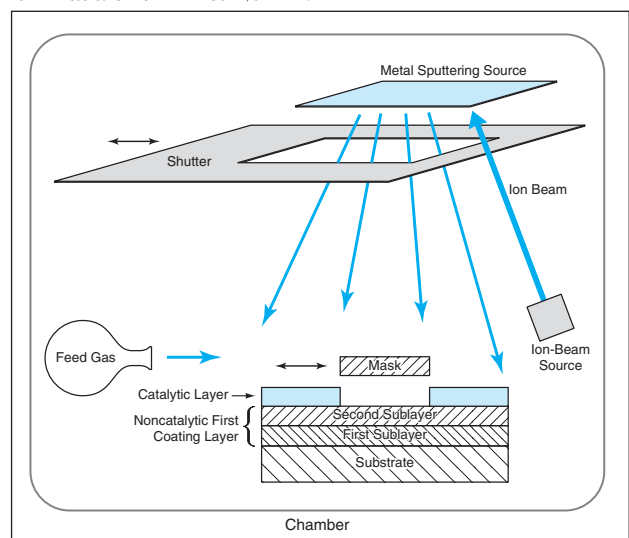
The figure schematically depicts salient aspects of the method and apparatus in a typical application. A substrate is placed in a chamber that contains both ion-beam sputtering and CVD equipment. The substrate can be made of any of a variety of materials that include several forms of silicon or carbon, and selected polymers, metals, ceramics, and even some natural minerals and similar materials. Optionally, the substrate is first coated with a non-catalytic metal layer (which could be a single layer or could comprise multiple different sublayers) by ion-beam sputtering. The choice of metal(s) and thickness(es) of the first layer (if any) and its sublayers (if any) depends on the chemical and electrical properties required for subsequent deposition of

the catalyst and the subsequent CVD of the carbon nanotubes.

A typical first-sublayer metal is Pt, Pd, Cr, Mo, Ti, W, or an alloy of two or more of these elements. A typical metal for the second sublayer or for an undivided first layer is Al at a thickness  $\geq 1$  nm or Ir at a thickness  $\geq 5$  nm. Proper choice of the metal for a second sublayer of a first layer makes it possible to use a catalyst that is chemically incompatible with the substrate.

In the next step, a mask having holes in the desired pattern is placed over the coated substrate. The catalyst is then deposited on the coated substrate by ion-beam sputtering through the mask. Optionally, the catalyst could be deposited by a technique other than sputtering and/or pat-

terned by use of photolithography, electron-beam lithography, or another suitable technique. The catalytic metal can be Fe, Co, Ni, or an alloy of two or more of these elements, deposited to a typical thickness in the range from 0.1 to 20 nm.



This Schematic Diagram represents a composite of the apparatus as configured for the catalyst-patterning and CVD steps of the method.

Following deposition of the patterned catalyst, a shutter is moved into place to protect the sputtering equipment against CVD of carbon, then a hydrocarbon feed gas (primarily CH<sub>4</sub>, C<sub>2</sub>H<sub>2</sub>, or C<sub>2</sub>H<sub>4</sub>) heated to a suitable temperature is admitted into the chamber. Optionally, the feed gas can be part of a mixture that includes an inert carrier gas. The heated feed gas decomposes into hydrogen and carbon, with deposition of the carbon on the cata-

lyst. Whether what are grown are single-walled nanotubes (SWNTs), multi-walled nanotubes (MWNTs), or nanofibers depends primarily on the feed gas and temperature used in CVD and secondarily on the structures and compositions of the first layer and the patterned catalytic second layer. For example, for growing SWNTs, the preferred gas is CH<sub>4</sub> and the preferred temperature is ≈900 °C. For growing MWNTs, the preferred gas is C<sub>2</sub>H<sub>2</sub> or

C<sub>2</sub>H<sub>4</sub>, the preferred temperature is ≈750 °C. For growing nanofibers, it is preferable to form a plasma discharge in the chamber and to maintain the temperature between 400 and 700 °C.

*This work was done by Lance D. Delzeit of Ames Research Center. Further information is contained in a TSP (see page 1).*

*Inquiries concerning rights for the commercial use of this invention should be addressed to the Patent Counsel, Ames Research Center, (650) 604-5104. Refer to ARC-14613.*

---

## **Lightweight, Rack-Mountable Composite Cold Plate/Shelves**

*Lyndon B. Johnson Space Center, Houston, Texas*

Rack-mountable composite-material structural components that would serve as both shelves and cold plates for removing heat from electronic or other equipment mounted on the shelves have been proposed as lightweight alternatives to all-metal cold plate/shelves now in use. A proposed cold plate/shelf would include a highly thermally conductive face sheet containing oriented graphite fibers bonded to an aluminum honeycomb core, plus an extruded stainless-steel substructure containing optimized flow passages for a cooling fluid, and an inlet and outlet that could be

connected to standard manifold sections. To maximize heat-transfer efficiency, the extruded stainless-steel substructure would be connected directly to the face sheet. On the basis of a tentative design, the proposed composite cold plate/shelf would weigh about 38 percent less than does an all-aluminum cold plate in use or planned for use in some spacecraft and possibly aircraft. Although weight is a primary consideration, the tentative design offers the additional benefit of reduction of thickness to half that of the all-aluminum version.

*This work was done by Kathryn M. Hurl-*

*bert of Johnson Space Center and Warren Ruennele, Hai D. Nguyen, Kambiz K. Andish, and Sean McCalley of Lockheed Martin.*

*Title to this invention has been waived under the provisions of the National Aeronautics and Space Act {42 U.S.C. 2457(f)}, to Lockheed Martin Space Operations. Inquiries concerning licenses for its commercial development should be addressed to:*

*Lockheed Martin Space Operations*

*2400 NASA Road 1*

*Nassau Bay, TX 77058*

*Refer to MSC-23160, volume and number of this NASA Tech Briefs issue, and the page number.*

## SiC-Based Miniature High-Temperature Cantilever Anemometer

This compact, minimally intrusive sensor functions at temperature as high as 600 °C.

*John H. Glenn Research Center, Cleveland, Ohio*

The figure depicts a miniature cantilever-type anemometer that has been developed as a prototype of compact, relatively nonintrusive anemometers that can function at temperatures up to 600 °C and that can be expected to be commercially mass-producible at low cost. The design of this anemometer, and especially the packaging aspect of the design, is intended to enable measurement of turbulence in the high-temperature, high-vibration environment of a turbine engine or in any similar environment.

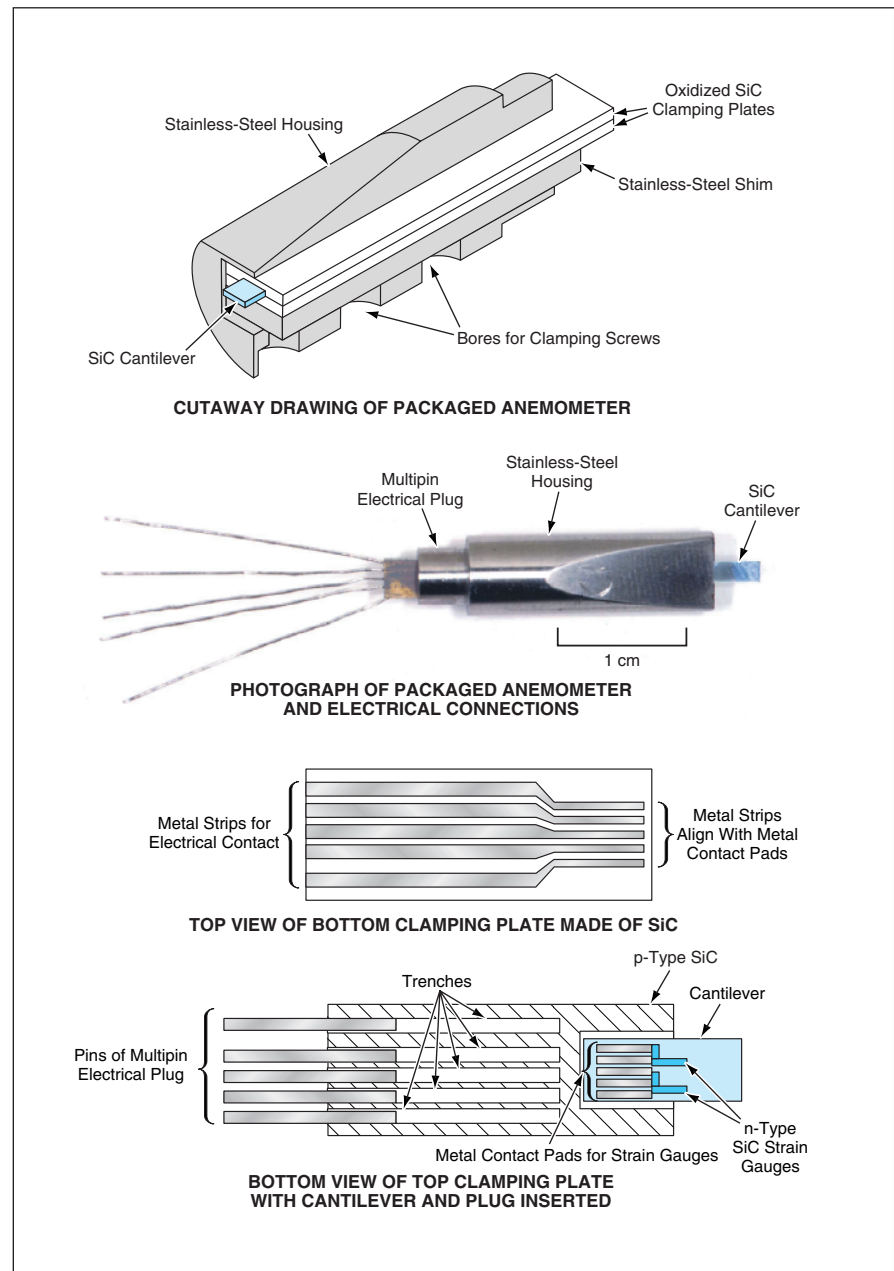
The main structural components of the anemometer include a single-crystal SiC cantilever and two polycrystalline SiC clamping plates, all made from chemical-vapor-deposited silicon carbide. Fabrication of these components from the same basic material eliminates thermal-expansion mismatch, which has introduced spurious thermomechanical stresses in cantilever-type anemometers of prior design.

The clamping plates are heavily oxidized to improve electrical insulation at high temperature. A cavity that serves as a receptacle for the clamped end of the cantilever is etched into one end of one clamping plate. Trenches that collectively constitute a socket for a multipin electrical plug (for connection to external electronic circuitry) are etched into the opposite end of this clamping plate. Metal strips for electrical contact are deposited on one face of the other clamping plate. Piezoresistive single-crystal SiC thin-film strain gauges are etched in the n-type SiC epilayer in a Wheatstone-bridge configuration. Metal contact pads on the cantilever that extend into the clamping-receptacle area, are obtained by deposition and patterning using standard semiconductor photolithography and etching methods.

The cantilever and the two clamping plates are assembled into a sandwich structure that is then clamped in a stainless-steel housing. The Wheatstone-bridge carrying SiC cantilever with the metal contact pads on the piezoresistors is slid into the receptacle in the bottom clamping plate. The top

clamping plate is brought into contact with the bottom plate so that the narrow section of the metal strips on the top clamp plate aligns with the metal contact pads on the cantilever. When the parts are clamped together, the

metal strips provide electrical connections between the Wheatstone-bridge contact points and the sides the trenches that constitute the socket for the multipin electrical plug. Hence, to connect the Wheatstone bridge to ex-



This **Cantilever-Type Anemometer** is an integral combination of functional and packaging components that, together, afford the ability to withstand high temperature, "plug-and-play" functionality, and mass-producibility.

ternal circuitry for processing of the anemometer readout, one need only insert the plug in the socket.

In operation, the cantilever end of the stainless-steel housing is mounted flush with an engine wall and the unclamped portion of the cantilever is exposed into the flow. The cantilever is deflected in direct proportion to the force induced by component of flow parallel to the en-

gine wall and perpendicular to the broad exposed face of the cantilever. The maximum strain on the cantilever occurs at the clamped edge and is measured by the piezoresistors, which are located there. The corresponding changes in resistance manifest themselves in the output of the Wheatstone bridge.

*This work was done by Robert S. Okojie, Gustave Fralick, and George J. Saad of*

**Glenn Research Center.** *Further information is contained in a TSP (see page 1).*

*Inquiries concerning rights for the commercial use of this invention should be addressed to NASA Glenn Research Center, Commercial Technology Office, Attn: Steve Fedor, Mail Stop 4-8, 21000 Brookpark Road, Cleveland, Ohio 44135. Refer to LEW-17222.*

---

## Inlet Housing for a Partial-Admission Turbine

**The housing is shaped to smooth the inlet flow.**

*Marshall Space Flight Center, Alabama*

An inlet housing for a partial-admission turbine has been designed to cause the inlet airflow to make a smooth transition from an open circular inlet to an inlet slot. The smooth flow is required for purposes of measuring inlet flow characteristics and maximizing the efficiency of the turbine.

A partial-admission turbine is a turbine in which the inlet slot occupies less than a complete circle around the rotor axis. In this case, the inlet slot occupies a 90° arc. The present special inlet-housing design is needed because the “bull nose” shape of a conventional turbine inlet housing fails to provide the required smooth transition in a partial-admission configuration and thereby gives

rise to a loss of turbine efficiency and inaccuracies in inlet flow measurements.

Upon entering the inlet housing through the circular opening, the flow encounters a “tongue”-shaped passageway, which serves as a ramp that diverts the flow to the first of two straight passages. This first passageway occupies a 90° arc and has a length equal to two passage heights. Instrumentation rakes for measuring the characteristics of the inlet flow are installed in this passageway.

Just past the first straight passageway is the second one, which is narrower and leads to the 90° turbine inlet slot. This passageway is used to smooth the flow immediately prior to its passage through the turbine inlet slot. The length of this

second passageway equals the length of the chord of a turbine vane.

The inlet housing incorporates small ports for measuring static pressures at various locations of the flow, and incorporates bosses for the installation of the instrumentation rakes. The inlet housing also includes a flange at its inlet end for attachment to a circular inlet duct and a flange at its outlet end for attachment to the outer casing of the turbine.

*This work was done by Ralph Moyer, William Myers, and Kevin Baker of Marshall Space Flight Center.* *Further information is contained in a TSP (see page 1).*  
*MFS-31971*

## Lightweight Thermoformed Structural Components and Optics

Precise shapes can be replicated.

*Marshall Space Flight Center, Alabama*

A technique that involves the use of thermoformed plastics has been developed to enable the design and fabrication of ultra-lightweight structural components and mirrors for use in outer space. The technique could also be used to produce items for special terrestrial uses in which minimization of weight is a primary design consideration.

Although the inherent strengths of thermoplastics are clearly inferior to those of metals and composite materials, thermoplastics offer a distinct advantage in that they can be shaped, at elevated temperatures, to replicate surfaces (e.g., prescribed mirror surfaces) precisely. Furthermore, multiple elements can be bonded into structures of homogeneous design that display minimal thermal deformation aside from simple expansion.

The design aspect of the present technique is based on the principle that the deflection of a plate that has internal

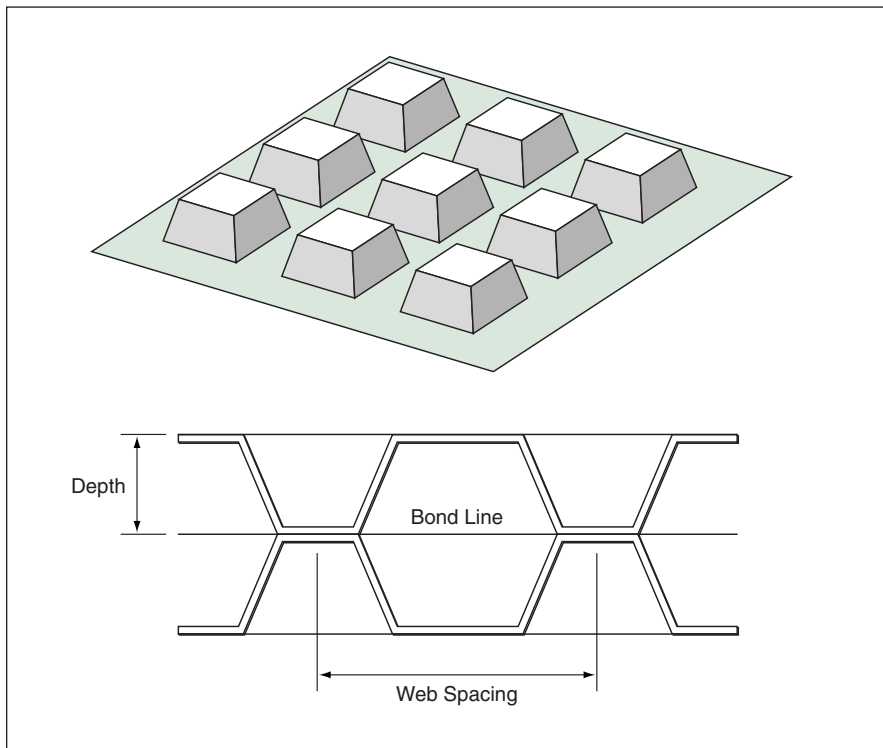
structure depends far more on the overall thickness than on the internal details; thus, a very stiff, light structure can be made from thin plastic that is heat-formed to produce a sufficiently high moment of inertia. General examples of such structures include I beams and eggcrates.

For a more specific example, consider an eggcrate-like structure made from a polyimide film with a thickness of 5 mils (0.13 mm) [corresponding to an areal density of 0.175 kg/m<sup>2</sup>]. The initially flat film can be locally elongated by >200 percent at a temperature of 300 °C, to produce a structure with a depth ≈70 percent of the two-dimensional web spacing (see figure). Such structures have been successfully fabricated by use of a pressurized machined mold. A particularly attractive configuration results when a mold is cross milled to produce truncated pyramidal posts as shown in the figure. The top faces of the posts of two molded sheets

are then bonded to produce a strong, lightweight panel. A 10-cm-diameter disk panel made in this configuration and optimally supported at three points would undergo a root-mean-square deflection of less than 10 nm under its own weight under normal Earth gravitation. At 10<sup>-4</sup> × normal Earth gravitation, a disk panel of 1-m diameter but otherwise the same design would be deflected by the same amount.

It has been shown that a precise mirror (which can be curved or flat) can be formed by replication, with minimal "printthrough," in a mirror face sheet of thermoplastic. An initially flat sheet of thermoplastic destined to become the mirror face sheet is placed on a mold surface shaped in the exact opposite ("mirror image") of the desired optical figure. Then a supporting structure of a lightweight design like the one described above is bonded to the rear surface of the mirror face sheet under pressure at elevated temperature. Either the face sheet can have been pre-metallized for high reflectivity, or else a reflective layer can be vacuum-deposited on the face sheet after fabrication. The web spacing of the support structure in this case would be matched to the thickness of the face sheet to yield an acceptably low level of deformation: Typically, in the case of 5-mil (0.13-mm)-thick face sheet, the web spacing for submicron deflection under normal Earth gravitation would be ≈1 cm, while the web spacing for submicron deflection at 10<sup>-4</sup> × normal Earth gravitation would be ≈10 cm. Such a mirror composed of three 5-mil sheets would have an areal density of 0.525 kg/m<sup>2</sup> but the density could conceivably be reduced to as little as 0.125 kg/m<sup>2</sup> by use of 1-mil (0.025-mm) sheets instead.

*This work was done by Glenn W. Zeiders of the Sirius Group and Larry J. Bradford of the CAT Flight Services, Inc., for Marshall Space Flight Center. For further information, contact the Sirius Group, 2803 Downing Court, Huntsville, AL 35801, Telephone No.: (256) 650-5234. MFS-31412*

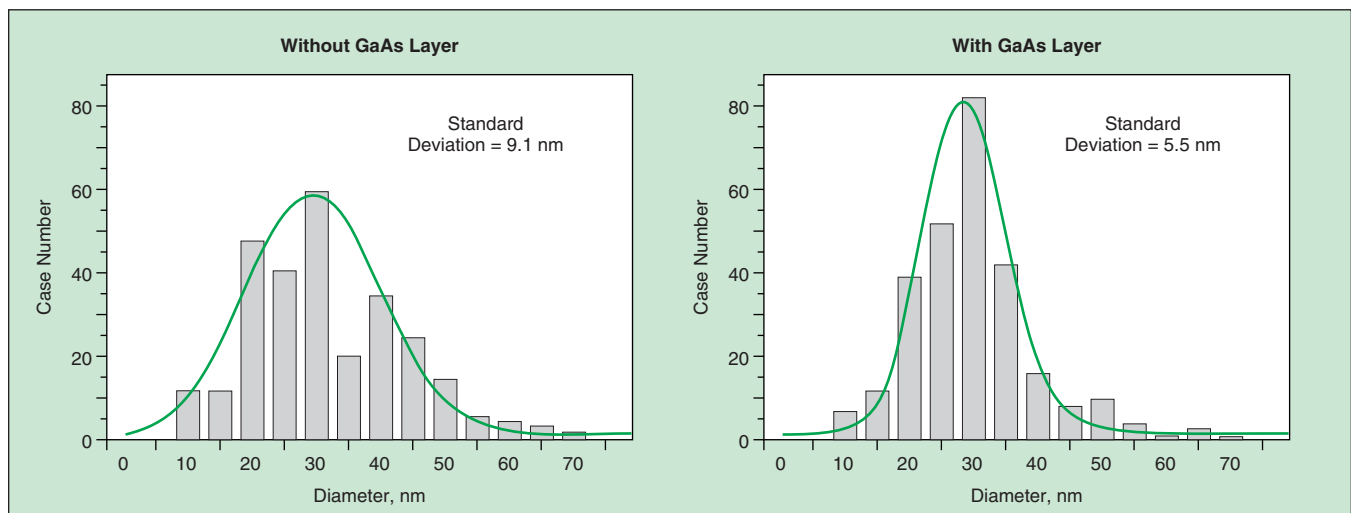


Thin Sheets of Plastic Are Thermoformed into eggcrate-like components, which are then bonded together to produce a stiff, lightweight structure.

# Growing High-Quality InAs Quantum Dots for Infrared Lasers

A deposition process has been modified to grow more nearly uniform quantum dots.

NASA's Jet Propulsion Laboratory, Pasadena, California



The **Distribution of Sizes** of InAs quantum dots is narrower (in other words, the dots are more nearly uniform) when a thin layer of GaAs is deposited before the quantum dots are deposited.

An improved method of growing high-quality InAs quantum dots embedded in lattice-matched InGaAs quantum wells on InP substrates has been developed. InAs/InGaAs/InP quantum dot semiconductor lasers fabricated by this method are capable of operating at room temperature at wavelengths  $\geq 1.8 \mu\text{m}$ . Previously, InAs quantum dot lasers based on InP substrates have been reported only at low temperature of 77 K at a wavelength of 1.9  $\mu\text{m}$ .

In the present method, as in the prior method, one utilizes metalorganic vapor phase epitaxy to grow the afore-

mentioned semiconductor structures. The development of the present method was prompted in part by the observation that when InAs quantum dots are deposited on an InGaAs layer, some of the InAs in the InGaAs layer becomes segregated from the layer and contributes to the formation of the InAs quantum dots. As a result, the quantum dots become highly nonuniform; some even exceed a critical thickness, beyond which they relax.

In the present method, one covers the InGaAs layer with a thin layer of

GaAs before depositing the InAs quantum dots. The purpose and effect of this thin GaAs layer is to suppress the segregation of InAs from the InGaAs layer, thereby enabling the InAs quantum dots to become nearly uniform (see figure). Devices fabricated by this method have shown near-room-temperature performance.

*This work was done by Yueming Qiu and David Uhl of Caltech for NASA's Jet Propulsion Laboratory. Further information is contained in a TSP (see page 1). NPO-30903*



## Selected Papers on Protoplanetary Disks

Ames Research Center, Moffett Field, California

Three papers present studies of thermal balances, dynamics, and electromagnetic spectra of protoplanetary disks, which comprise gas and dust orbiting young stars. One paper addresses the re-processing, in a disk, of photons that originate in the disk itself in addition to photons that originate in the stellar object at the center. The shape of the disk is found to strongly affect the redistribution of energy. Another of the three papers reviews an increase in the optical luminosity of the young star FU Orionis. The increase

began in the year 1936 and similar increases have since been observed in other stars. The paper summarizes astronomical, meteoric, and theoretical evidence that these increases are caused by increases in mass fluxes through the inner portions of the protoplanetary disks of these stars. The remaining paper presents a mathematical-modeling study of the structures of protostellar accretion disks, with emphasis on limits on disk flaring. Among the conclusions reached in the study are that (1) the radius at which

a disk becomes shadowed from its central stellar object depends on radial mass flow and (2) most planet formation has occurred in environments unheated by stellar radiation.

*This work was done by K. R. Bell and P. M. Cassen of Ames Research Center, J. T. Wasson and D. S. Woolum of the University of California, and H. H. Klahr and Th. Henning of the Max Planck Society (Jena, Germany). Further information is contained in a TSP (see page 1). ARC-14986*

## Module for Oxygenating Water Without Generating Bubbles

No bubbles were observed at any of the test flow rates.

Lyndon B. Johnson Space Center, Houston, Texas

A module that dissolves oxygen in water at concentrations approaching saturation, without generating bubbles of oxygen gas, has been developed as a prototype of improved oxygenators for water-disinfection and water-purification systems that utilize photocatalyzed redox reactions. Depending on the specific nature of a water-treatment system, it is desirable to prevent the formation of bub-

bles for one or more reasons: (1) Bubbles can remove some organic contaminants from the liquid phase to the gas phase, thereby introducing a gas-treatment problem that complicates the overall water-treatment problem; and/or (2) in some systems (e.g., those that must function in microgravity or in any orientation in normal Earth gravity), bubbles can interfere with the flow of the liquid phase.

The present oxygenation module (see Figure 1) is a modified version of a commercial module that contains >100 hollow polypropylene fibers with a nominal pore size of 0.05  $\mu\text{m}^2$ . The module was originally designed for oxygenation in a bioreactor, with no water flowing around or inside the tubes. The modification, made to enable the use of the module to oxygenate

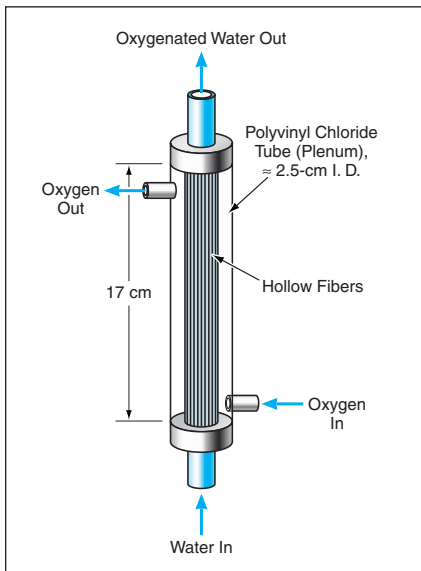


Figure 1. Hollow, Porous Polypropylene Fibers contain flowing water. Oxygen diffuses through the fiber walls and is dissolved in the water.

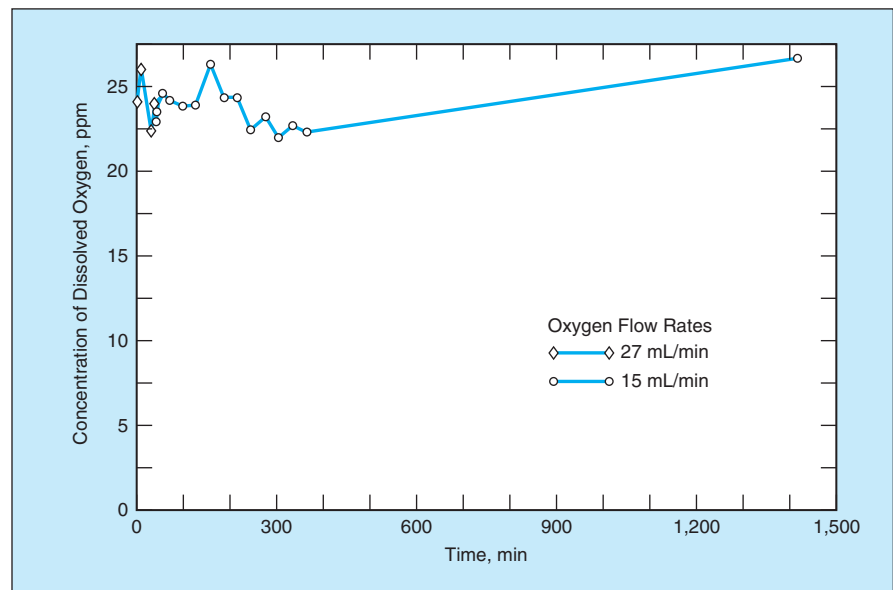


Figure 2. The Concentration of Dissolved Oxygen as a function of time was measured with water flowing through the module at a rate of 300 mL and with two different oxygen-flow rates.

flowing water, consisted mainly in the encapsulation of the fibers in a tube of Tygon polyvinyl chloride (PVC) with an inside diameter of 1 in. ( $\approx 25$  mm). In operation, water is pumped along the insides of the hollow fibers and oxygen gas is supplied to the space outside the hollow tubes inside the PVC tube.

In tests, the pressure drops of water and oxygen in the module were found to be close to zero at water-flow rates ranging up to 320 mL/min and oxygen-flow rates up to 27 mL/min. Under all test conditions, no bubbles were observed at

the water outlet. In some tests, flow rates were chosen to obtain dissolved-oxygen concentrations between 25 and 31 parts per million (ppm) — approaching the saturation level of  $\approx 35$  ppm at a temperature of 20 °C and pressure of 1 atm ( $\approx 0.1$  MPa).

As one would expect, it was observed that the time needed to bring a flow of water from an initial low dissolved-oxygen concentration (e.g., 5 ppm) to a steady high dissolved-oxygen concentration at or near the saturation level depends on the rates of flow of both oxy-

gen and water, among other things. Figure 2 shows the results of an experiment in which a greater flow of oxygen was used during the first few tens of minutes to bring the concentration up to  $\approx 25$  ppm, then a lesser flow was used to maintain the concentration.

*This work was done by Anuncia Gonzalez-Martin, Reyinjan Sidik, and Jinseong Kim of Lynntech, Inc., for Johnson Space Center. For further information, contact the Johnson Commercial Technology Office at (281) 483-3809. MSC-23138*

## Coastal Research Imaging Spectrometer

**Color and temperature images yield information on contents and sources of flows.**

*Stennis Space Center, Mississippi*

The Coastal Research Imaging Spectrometer (CRIS) is an airborne remote-sensing system designed specifically for research on the physical, chemical, and biological characteristics of coastal waters. The CRIS includes a visible-light hyperspectral imaging subsystem for measuring the color of water, which contains information on the biota, sediment, and nutrient contents of the water. The CRIS also includes an infrared imaging subsystem, which provides information on the temperature of the water. The combination of measurements enables investigation of biological effects of both natural and artificial flows of water from land into the ocean, including diffuse and point-source flows that may contain biological and/or chemical pollutants.

Temperature is an important element of such measurements because temperature contrasts can often be used to distinguish among flows from different sources: for example, a sewage outflow could manifest itself in spectral images as a local high-temperature anomaly.

Both the visible and infrared subsystems scan in “pushbroom” mode: that is, an aircraft carrying the system moves along a ground track, the system is aimed downward, and image data are acquired in across-track linear arrays of pixels. Both subsystems operate at a frame rate of 30 Hz. The infrared and visible-light optics are adjusted so that both subsystems are aimed at the same moving swath, which has across-track angular width of 15°. Data from the in-

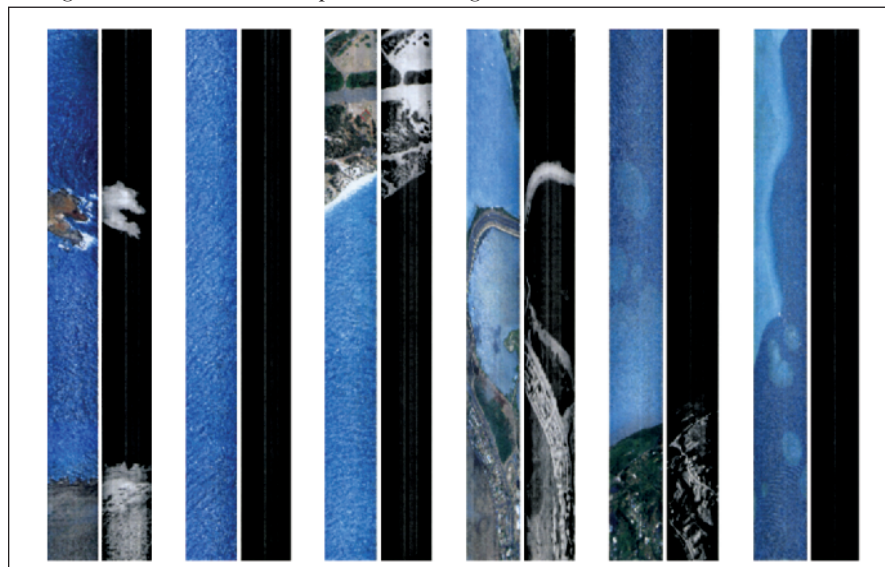
frared and visible imaging subsystems are stored in the same file along with aircraft-position data acquired by a Global Positioning System receiver. The combination of the three sets of data is used to construct infrared and hyperspectral maps of scanned areas (see figure).

The visible subsystem is based on a grating spectrograph and a rapid-readout charge-coupled-device camera. Images of the swath are acquired in 256 spectral bands at wavelengths from 400 to 800 nm. The infrared subsystem, which is sensitive in a single wavelength band of 8 to 10  $\mu\text{m}$ , is based on a focal-plane array of HgCdTe photodetectors that are cooled to an operating temperature of 77 K by use of a closed-Stirling-cycle mechanical cooler.

The nonuniformities of the HgCdTe photodetector array are small enough that the raw pixel data from the infrared subsystem can be used to recognize temperature differences on the order of 1 °C. By use of a built-in blackbody calibration source that can be switched into the field of view, one can obtain bias and gain offset terms for individual pixels, making it possible to offset the effects of nonuniformities sufficiently to enable the measurement of temperature differences as small as 0.1 °C.

*This work was done by Paul G. Lucey, Timothy Williams, and Keith A. Horton of Pacific Island Technology, Inc., for Stennis Space Center.*

*Inquiries concerning rights for the commercial use of this invention should be addressed to the Intellectual Property Manager, Stennis Space Center, (228) 688-1929. Refer to SSC-00158*



These **Color and Monochrome Images** of the same ocean areas were generated from outputs of the visible-light hyperspectral and infrared subsystem, respectively, of the CRIS during its test flight.

# Rapid Switching and Modulation by Use of Coupled VCSELs

With proper design, coupled VCSELs oscillate at tens of gigahertz.

Ames Research Center, Moffett Field, California

Devices incorporating coupled vertical-cavity surface-emitting lasers (VCSELs) have been proposed as means to effect unprecedentedly rapid modulation and/or switching of light beams in advanced optical communication and

information-processing systems. A basic device according to the proposal would comprise two or more VCSELs (1) positioned so close to each other that they are coupled and (2) connected to a current source that biases them at a steady

current above the threshold current for lasing.

The operation of VCSELs under the conditions stated above has been simulated computationally with an algorithm that solves an approximation of the Maxwell-Bloch equations. (These are nonlinear coupled partial differential equations that model the relevant aspects of the physics of semiconductor lasers.) The results of the simulations show that the intensities of the beams oscillate, out of phase relative to each other, at a frequency that is typically of the order of tens of gigahertz.

In particular, one simulation was performed for two coupled VCSELs, each having a circular aperture  $5.6 \mu\text{m}$  in diameter, operating at a wavelength of  $980 \text{ nm}$ . The results of the simulation showed that the intensities of the two beams oscillated in opposite phase (see Figure 1) at a frequency of  $42 \text{ GHz}$ . In the far field, the beams were found to be separated by an angle of  $\approx 8^\circ$ . The intensities of the beams were also found to oscillate in the near field,  $90^\circ$  out of phase with the oscillation in the far field. Figure 2 depicts a simple near-field switching device in which an assembly of microlenses would couple the two oscillating beams to two receivers.

Other simulations were performed to investigate the effects of VCSEL geometry and injection current on the oscillation frequency, relative brightness, and separation of the beams. In one simulation, for example, it was found that two VCSELs having square apertures would oscillate at  $50 \text{ GHz}$  with a beam pattern similar to that of two VCSELs having circular apertures. In another simulation, it was found that for three round VCSELs arranged around a ring, the far field would move in a circular pattern at a frequency of  $31 \text{ GHz}$ . In yet another simulation, the far-field pattern of four round VCSELs arranged in a square would comprise two circular-cross-section beams oscillating spatially in opposite directions at a frequency of  $50 \text{ GHz}$ .

*This work was done by Peter M. Goorjian and Cun-Zhen Ning of Ames Research Center. Further information is contained in a TSP (see page 1).*

*Inquiries concerning rights for the commercial use of this invention should be addressed to the Patent Counsel, Ames Research Center, (650) 604-5104. Refer to ARC-14682.*

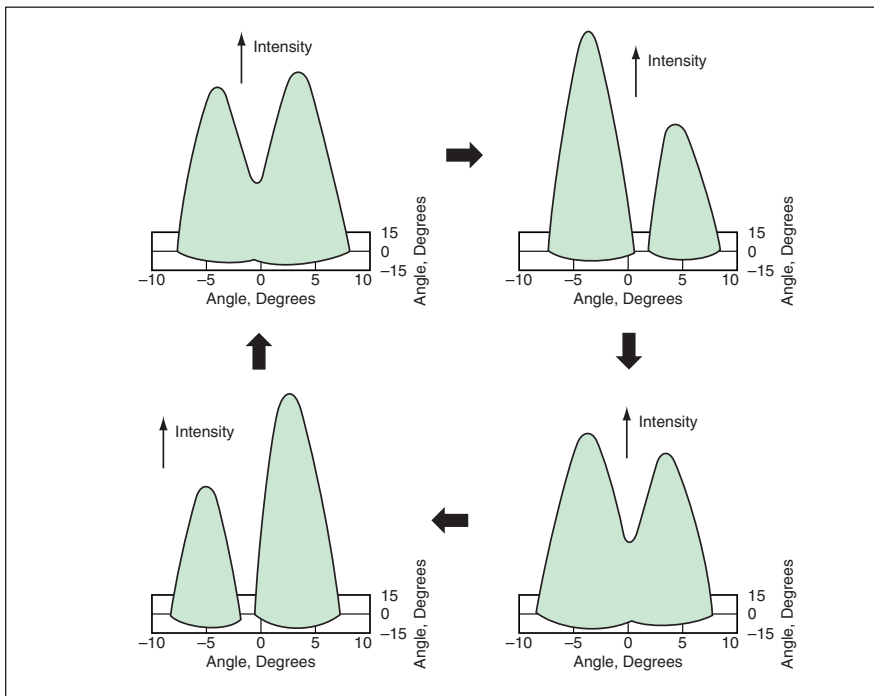


Figure 1. These Plots of Intensity Versus Polar Angles, generated by computational simulation, are snapshots at selected intervals of one cycle of oscillation of the beams from two coupled VCSELs.

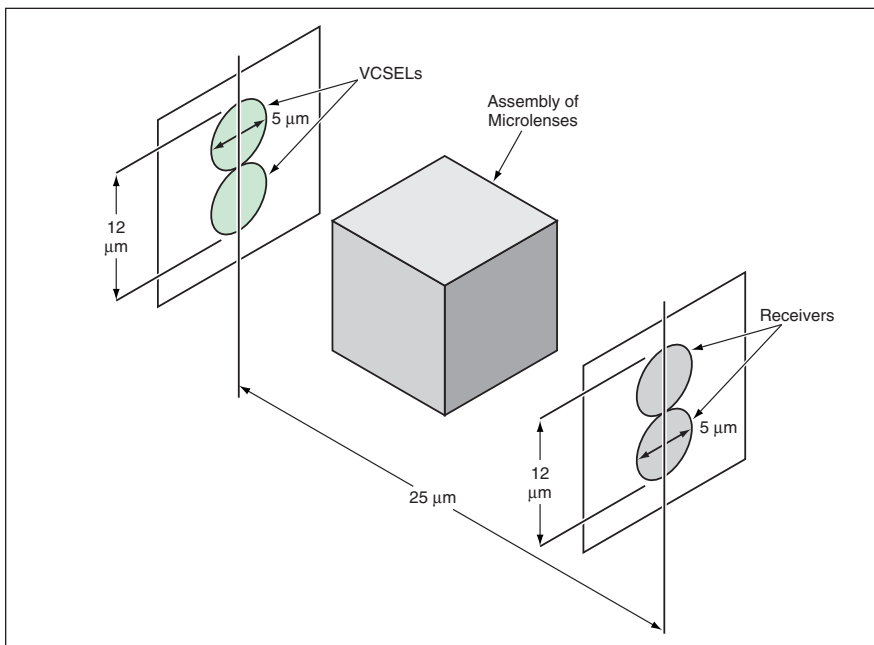


Figure 2. The Assembly of Microlenses would couple the oscillating beams from two coupled VCSELs to two receivers.

# Laser-Induced-Fluorescence Photogrammetry and Videogrammetry

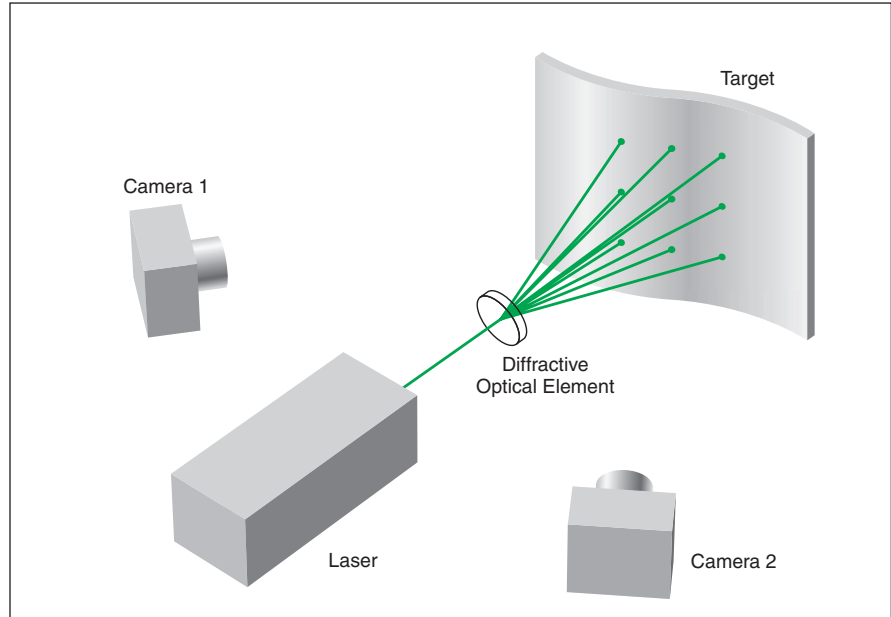
Signal-to-noise ratios are enhanced and effects of laser speckle suppressed.

Langley Research Center, Hampton, Virginia

An improved method of dot-projection photogrammetry and an extension of the method to encompass dot-projection videogrammetry overcome some deficiencies of dot-projection photogrammetry as previously practiced. The improved method makes it possible to perform dot-projection photogrammetry or videogrammetry on targets that have previously not been amenable to dot-projection photogrammetry because they do not scatter enough light. Such targets include ones that are transparent, specularly reflective, or dark.

In standard dot-projection photogrammetry, multiple beams of white light are projected onto the surface of an object of interest (denoted the target) to form a known pattern of bright dots. The illuminated surface is imaged in one or more cameras oriented at a nonzero angle or angles with respect to a central axis of the illuminating beams. The locations of the dots in the image(s) contain stereoscopic information on the locations of the dots, and, hence, on the location, shape, and orientation of the illuminated surface of the target. The images are digitized and processed to extract this information. Hardware and software to implement standard dot-projection photogrammetry are commercially available.

Success in dot-projection photogrammetry depends on achieving sufficient signal-to-noise ratios: that is, it depends on scattering of enough light by the target so that the dots as imaged in the camera(s) stand out clearly against the ambient-illumination component of the image of the target. In one technique used previously to increase the signal-to-noise ratio, the target is illuminated by intense, pulsed laser light and the light entering the camera(s) is band-pass filtered at the laser wavelength. Unfortunately, speckle caused by the coherence of the laser light engenders apparent movement in the projected dots, thereby giving rise to errors in the measurement of the centroids of the dots and corresponding errors in the computed shape and location of the surface of the target.



A Laser Beam Is Split into multiple beams to form dots of illumination on a target. The dots are observed by use of stereoscopic cameras.

The improved method is denoted laser-induced-fluorescence photogrammetry. In preparation for observation by this method, a target is made fluorescent by whichever of several techniques is most appropriate. Examples include the following:

- A target sheet or membrane (e.g., a membrane subject to deflections that one seeks to measure) made of a transparent or translucent polymer could be doped with a fluorescent dye during its manufacture. If, in addition, the target were coated on one side with metal to render it specularly reflective, then it could be positioned for photogrammetric observation of its uncoated side.
- A thick transparent, translucent, or dark opaque object (e.g., a wind-tunnel model, the position, orientation, and deflection of which one seeks to measure) could be doped with a fluorescent dye during its manufacture.
- A specularly reflective or dark object that has already been manufactured could be coated with a paint or lacquer containing a dissolved fluorescent dye.
- The surface of a part of a human body to be observed photogrammetrically could be coated painted or sprayed

with a harmless fluorescent dye in a nontoxic solvent.

- A fluorescent dye could be dissolved in a body of liquid, which could be, for example, water in a tank for experiments on the sizes, shapes, and motions of waves.

In this method, a laser beam is pulsed and is split into multiple beams by use of a commercially available diffractive optical element (see figure). The laser beams form dots of light on the target, exciting fluorescence in the dye. Unlike the laser light, the fluorescence from the dots is incoherent and therefore, there is no laser speckle in the fluorescence. Like scattered light, the fluorescent light is emitted in all directions.

The cameras are time-gated to acquire images only during the interval of maximum fluorescence following the laser pulse, to suppress the contribution of ambient light between pulses. To suppress ambient light further, the light entering the cameras is band-pass filtered at the fluorescence wavelength, which is longer than the laser wavelength. This filtering also blocks directly reflected laser light, which, if allowed to enter the cameras, could give rise to spurious dot images.

The extension of the method to videogrammetry is straightforward: The laser and cameras can be operated in a sequence of pulses to acquire a sequence of projected-dot images. The im-

ages, or the sets of location and shape data extracted from the images, can be used to synthesize a motion picture showing how the target surface moves and/or deflects over time.

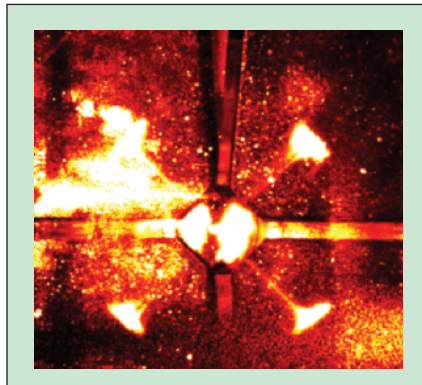
*This work was done by Paul Danehy, Tom Jones, John Connell, Keith Belvin, and Kent Watson of Langley Research Center. Further information is contained in a TSP (see page 1). LAR-16426*

## Laboratory Apparatus Generates Dual-Species Cold Atomic Beam

**A pyramidal magneto-optical trap extracts atoms from one chamber into another.**

*NASA's Jet Propulsion Laboratory, Pasadena, California*

A laser cooling apparatus that generates a cold beam of rubidium and cesium atoms at low pressure has been constructed as one of several intermediate products of a continuing program of research on laser cooling and atomic physics. Laser-cooled atomic beams, which can have temperatures as low as a microkelvin, have been used in diverse applications that include measurements of fundamental constants, atomic clocks that realize the international standard unit of time, atom-wave interferometers, and experiments on Bose-Einstein condensation. The present apparatus is a prototype of one being evaluated for use in a proposed microgravitational experiment called the Quantum Interferometric Test of Equivalence (QuITE). In this experiment, interferometric measurements of cesium and rubidium atoms in free fall would be part of a test of Einstein's equivalence principle. The present apparatus and its anticipated successors may also be useful in other experiments, in both microgravity and normal Earth gravity, in which there are requirements



This is a False-Color Image of fluorescence from cesium atoms in the pyramidal magneto-optical trap. The cold atomic beam in the extraction column is visible in the side views afforded by the 45° mirrors.

for dual-species atomic beams, low temperatures, and low pressures.

The apparatus includes a pyramidal magneto-optical trap in which the illumination is provided by multiple lasers tuned to frequencies characteristic of the two atomic species. The inlet to the apparatus is located in a vacuum chamber that con-

tains rubidium and cesium atoms at a low pressure; the beam leaving through the outlet of the apparatus is used to transfer the atoms to a higher-vacuum (lower-pressure) chamber in which measurements are performed.

The pyramidal magneto-optical trap is designed so that the laser cooling forces in one direction are unbalanced, resulting in a continuous cold beam of atoms that leak out of the trap (see figure). The radiant intensity (number of atoms per unit time per unit solid angle) of the apparatus is the greatest of any other source of the same type reported to date. In addition, this is the first such apparatus capable of producing a slow, collimated beam that contains two atomic species at the same time.

*This work was done by Robert Thompson, William Klipstein, James Kohel, Lute Maleki, Nathan Lundblad, Jaime Ramirez-Serrano, Dave Aveline, Nan Yu, and Daphna Enzer of Caltech for NASA's Jet Propulsion Laboratory. Further information is contained in a TSP (see page 1). NPO-30396*

## Laser Ablation of Materials for Propulsion of Spacecraft

*Marshall Space Flight Center, Alabama*

A report describes experiments performed as part of a continuing investigation of the feasibility of laser ablation of materials as a means of propulsion for small spacecraft. In each experiment, a specimen of ablative material was mounted on a torsion pendulum and irradiated with a laser pulse having an energy of 5 J. The amplitude of the resulting rotation of the torsion pendulum was taken to be an indication of the momentum transferred from the laser beam. Of the ablative materials tested, aluminum foils yielded the smallest rotation amplitudes — of the order of 10°. Black coating materials yielded rotation

amplitudes of the order of 90°. Samples of silver coated with a fluorinated ethylene propylene (FEP) copolymer yielded the largest rotation amplitudes — 6 to 8 full revolutions. The report presents a theory involving heating of a confined plasma followed by escape of the plasma to explain the superior momentum-transfer performance of the FEP specimens. It briefly discusses some concepts for optimizing designs of spacecraft engines to maximize the thrust obtainable by exploiting the physical mechanisms of the theory. Also discussed is the use of laser-ablation engines with other types of spacecraft engines.

*This work was done by David L. Edwards, Ralph Carruth, and Jonathan Campbell of Marshall Space Flight Center and Perry Gray of Native American Services.*

*In accordance with Public Law 96-517, the contractor has elected to retain title to this invention. Inquiries concerning rights for its commercial use should be addressed to*

*Native American Services, Inc.*

*3411 Triana Blvd. SW*

*Huntsville, AL 35805*

*Telephone No.: (256) 539-7928*

*Refer to MFS-31532, volume and number of this NASA Tech Briefs issue, and the page number.*

## Small Active Radiation Monitor

**This is a significant advancement over the passive dosimeters that presently monitor astronaut exposure to radiation.**

*Lyndon B. Johnson Space Center, Houston, Texas*

A device, named small active radiation monitor, allows on-orbit evaluations during periods of increased radiation, after extravehicular activities, or at predesignated times for crews on such long-duration space missions as on the International Space Station. It also permits direct evaluation of biological doses, a task now performed using a combination of measurements and potentially inaccurate simulations. Indeed the new monitor can measure a full array of radiation levels, from "soft" x-rays to "hard" galactic cosmic-ray particles. With refinement, it will benefit commercial (nuclear power-plant workers, airline pilots, medical technicians, physicians/dentists, and others) and military personnel as well as the astronauts for whom thermoluminescent dosimeters are inadequate.

Civilian and military personnel have long since graduated from film badges to thermoluminescent dosimeters. Once used, most dosimeters must be returned to a central facility for processing, a step that can take days or even weeks. While this suffices for radiation workers for whom exposure levels are typically very low and of brief duration, it does not work for astronauts. Even in emergencies and using express mail, the results can often be delayed by as much as 24 hours. Electronic dosimeters, which are the size of electronic oral thermometers, and tatters, small electronic dosimeters

that sound an alarm when the dose/dose rate exceeds preset values, are also used but suffer disadvantages similar to those of thermoluminescent dosimeters. None of these devices fully answers the need of rapid monitoring during the space missions. Instead, radiation is monitored by passive detectors, which are read out after the missions. Unfortunately, these detectors measure only the absorbed dose and not the biologically relevant dose equivalent.

The new monitor provides a real-time readout, a time history of radiation exposures (both absorbed dose and biologically relevant dose equivalent), and a count of the number of particles passing through a unit area. Better still, the monitor can be used anywhere. It is compact, measuring 8.3 by 4.8 by 1.9 cm, and has a solid-state diode and a thin protective coating that satisfy operational requirements — even at room temperature. Its preamplifier is a custom-made integrated circuit that has a range of approximately  $(6 \text{ to } 12,000) \times 10^{-15}$  coulombs, and the monitor can provide charge amplification, signal shaping, peak stretching, and adjustable discrimination. Its analog-to-digital converter is an 8-bit, tri-state output device that converts data in less than 1  $\mu$ s. Finally, it has a power-down mode capability and selectable lower and upper reference discrimination.

Eighty pins enable the small active radiation monitor to have multiple inputs and outputs, two clocks (one for timing and one for display), power-saving features (including standby and halt modes), and selectable instruction cycles (1 to 122  $\mu$ s). Each monitor is capable of running continuously, performing data dumps from the microprocessor to memory once every minute. Each data point includes the calendar time of measurement, the dose, and an estimated quality factor. Weighted quality factors are determined from a look-up table that has been programmed into the microprocessor's read-only memory. The new monitor is a sophisticated and vastly improved tool that is capable of supporting extended-duration stays on the Space Station as well as long-distance space explorations.

*This work was done by Gautam D. Badhwar of **Johnson Space Center** and Frank Gibbons of Lockheed Martin. For further information, contact:*

*NASA Lyndon B. Johnson Space Center  
Frank Gibbons/Mail code SF2  
2101 NASA Road One  
Houston, TX 77058  
E-mail: frank.l.gibbons@nasa.gov*

*Refer to MSC-22972, volume and number of this NASA Tech Briefs issue, and the page number.*

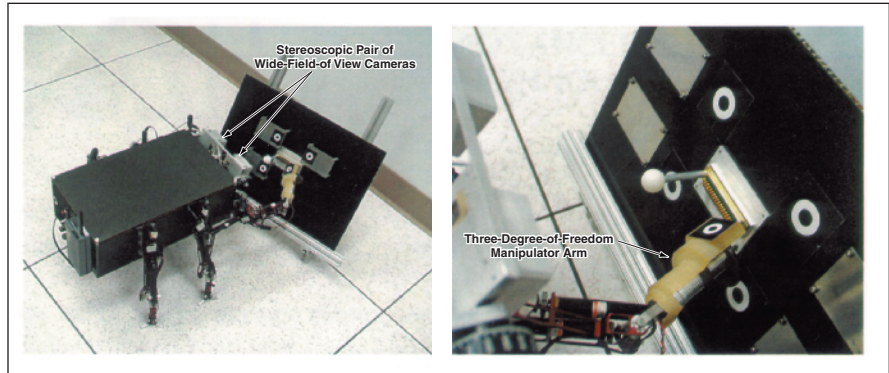
## Hybrid Image-Plane/Stereo Manipulation

This method is robust in the face of calibration errors.

NASA's Jet Propulsion Laboratory, Pasadena, California

Hybrid Image-Plane/Stereo (HIPS) manipulation is a method of processing image data, and of controlling a robotic manipulator arm in response to the data, that enables the manipulator arm to place an end-effector (an instrument or tool) precisely with respect to a target (see figure). Unlike other stereoscopic machine-vision-based methods of controlling robots, this method is robust in the face of calibration errors and changes in calibration during operation.

In this method, a stereoscopic pair of cameras on the robot first acquires images of the manipulator at a set of pre-defined poses. The image data are processed to obtain image-plane coordinates of known visible features of the end-effector. Next, there is computed an initial calibration in the form of a mapping between (1) the image-plane coordinates and (2) the nominal three-dimensional coordinates of the noted end-effector features in a reference frame fixed to the main robot body at the base of the manipulator. The nominal three-dimensional coordinates are obtained by use of the nominal forward kinematics of the manipulator arm — that is, calculated by use of the currently measured manipulator joint angles and previously measured lengths of manipulator arm segments under the assumption that the arm segments are rigid, that the arm lengths are constant, and that there is no backlash. It is un-



A Stereoscopic Pair of Electronic Cameras on a legged mobile exploratory robot acquires images of a scene that includes a manipulator arm and a target. The image data are used to guide the end effector of the manipulator toward the target.

derstood from the outset that these nominal three-dimensional coordinates are likely to contain possibly significant calibration errors, but the effects of the errors are progressively reduced, as described next.

As the end-effector is moved toward the target, the calibration is updated repeatedly by use of data from newly acquired images of the end-effector and of the corresponding nominal coordinates in the manipulator reference frame. By use of the updated calibration, the coordinates of the target are computed in manipulator-reference-frame coordinates and then used to the necessary manipulator joint angles to position and orient the end-effector at the target with respect to the

same kinematic model from the calibration step. As the end-effector/target distance decreases, the computed coordinates of the end-effector and target become more nearly affected by the same errors, so that the differences between their coordinates become increasingly precise. When the end-effector reaches the target, the remaining effective position error is the distance that corresponds to more than about one pixel in the stereoscopic images of the target.

*This work was done by Eric Baumgartner and Matthew Robinson of Caltech for NASA's Jet Propulsion Laboratory. Further information is contained in a TSP (see page 1).  
NPO-30492*

## Partitioning a Gridded Rectangle Into Smaller Rectangles

A relatively simple algorithm yields nearly square, nearly equally sized segments.

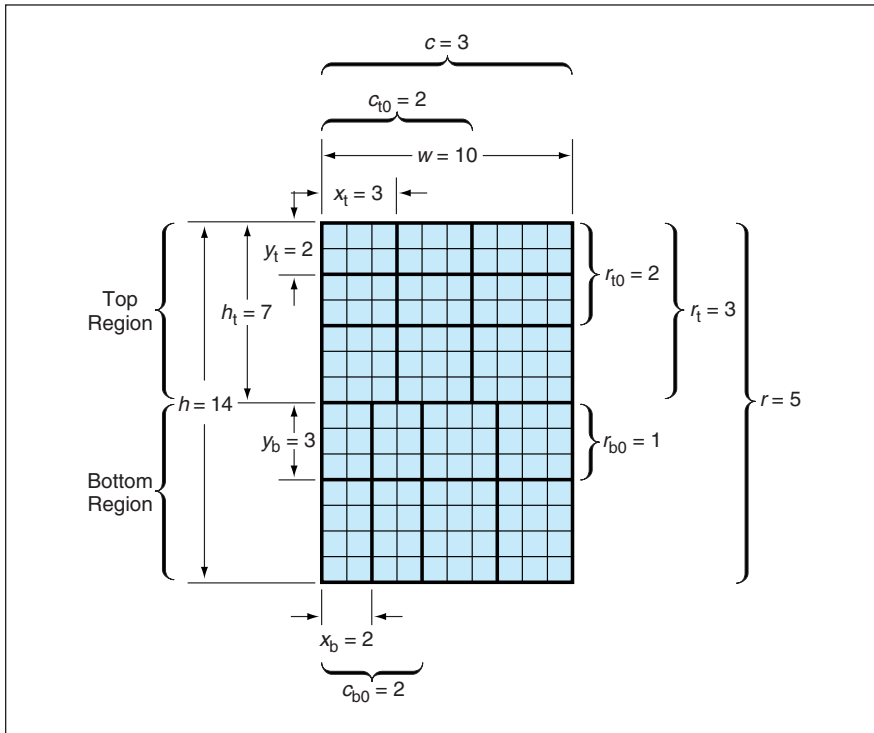
NASA's Jet Propulsion Laboratory, Pasadena, California

A relatively simple algorithm, devised for use in an image-data-compression application, partitions a rectangular pixelated image (or any other rectangle on which a regular rectangular grid has already been superimposed) into a specified number of smaller rectangles, hereafter denoted segments. The algorithm has the following properties:

- No floating-point operations are needed.
- The segments tend to be nearly square (in the sense that their widths and heights in pixel units tend to be nearly equal).
- The segments tend to have nearly equal areas.
- The algorithm yields valid results (no

zero-width or zero-height segments) as long as the specified number of segments,  $s$ , does not exceed the number of pixels (equivalently, the number of grid cells).

The inputs to the algorithm are the positive integer  $s$  plus the positive integers  $h$  and  $w$ , denoting the height and width, respectively, of the rectangle in



A Rectangular Image of 10 by 14 pixels is partitioned into 17 segments by the algorithm described in the text.

pixel units. The limit on  $s$  for a valid result is given by  $s \leq wh$ .

The output of the algorithm is characterized by, and can be described completely in terms of, several parameters that are illustrated by the example shown in the figure. The segments are arranged in  $r$  rows. A top region of the rectangle contains segments arranged in  $c$  columns. A possible bottom region contains segments arranged in  $c + 1$  columns. The top region has height  $h_t$  and contains  $r_t$  rows of segments. The first  $r_{t0}$  rows of segments in the top region have height  $y_t$ ; the remaining rows (if any) in the top

region have height  $y_t + 1$ . The first  $c_{t0}$  columns in the top region have width  $x_t$ ; any remaining columns in the top region have width  $x_t + 1$ . Similarly, the first  $r_{b0}$  rows in the bottom region have height  $y_b$ , and the remaining rows in the bottom region have height  $y_b + 1$ , while the first  $c_{b0}$  columns in the bottom region have width  $x_b$  and the remaining columns in the bottom region have width  $x_b + 1$ .

The steps of the algorithm are the following: First,  $r$  is computed. If  $h > (s-1)w$  then  $r = s$ . Otherwise,  $r$  is the unique positive integer that satisfies

$$(r-1)rw < hs \leq (r+1)rw.$$

Some of the other parameters are computed as follows:

$$c = \left\lfloor \frac{s}{r} \right\rfloor$$

$$r_t = (c+1)r - s$$

$$h_t = \max \left( r_t, \left\lfloor \frac{hcr_t}{s} + \frac{1}{2} \right\rfloor \right)$$

$$x_t = \left\lfloor \frac{w}{c} \right\rfloor$$

$$c_{t0} = (x_t + 1)c - w$$

$$y_t = \left\lfloor \frac{h_t}{r_t} \right\rfloor$$

$$r_{t0} = (y_t + 1)r_t - h_t.$$

If  $r_t < r$ , so that there is a bottom region, then the remaining parameters are computed as follows:

$$x_b = \left\lfloor \frac{w}{c+1} \right\rfloor$$

$$c_{b0} = (x_b + 1)(c+1) - w$$

$$y_b = \left\lfloor \frac{h - h_t}{r - r_t} \right\rfloor$$

$$r_{b0} = (y_b + 1)(r - r_t + 1) - (h - h_t).$$

It has been verified by straightforward algebraic analysis of these equations that the algorithm has the properties mentioned in the first paragraph.

*This work was done by Matthew Klimesh and Aaron Kiely of Caltech for NASA's Jet Propulsion Laboratory. Further information is contained in a TSP (see page 1).*

*This software is available for commercial licensing. Please contact Don Hart of the California Institute of Technology at (818) 393-3425. Refer to NPO-30479.*

## Digital Radar-Signal Processors Implemented in FPGAs

Processing can be performed onboard at relatively low power.

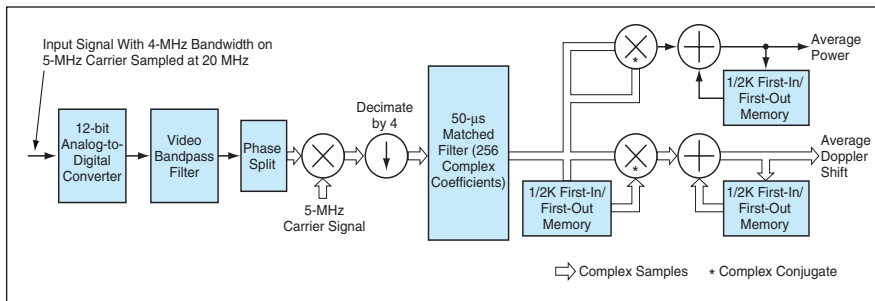
NASA's Jet Propulsion Laboratory, Pasadena, California

High-performance digital electronic circuits for onboard processing of return signals in an airborne precipitation-measuring radar system have been implemented in commercially available field-programmable gate arrays (FPGAs). Previously, it was standard practice to downlink the radar-return data to a ground station for postprocessing — a costly practice that

prevents the nearly-real-time use of the data for automated targeting. In principle, the onboard processing could be performed by a system of about 20 personal-computer-type microprocessors; relative to such a system, the present FPGA-based processor is much smaller and consumes much less power. Alternatively, the onboard processing could be performed by an application-specific

integrated circuit (ASIC), but in comparison with an ASIC implementation, the present FPGA implementation offers the advantages of (1) greater flexibility for research applications like the present one and (2) lower cost in the small production volumes typical of research applications.

The generation and processing of signals in the airborne precipitation-



The **Signal-Processing Functions** of one of the four channels require  $5 \times 10^9$  multiplications per second.

measuring radar system in question involves the following especially notable steps:

- The system utilizes a total of four channels — two carrier frequencies and two polarizations at each frequency.
- The system uses pulse compression: that is, the transmitted pulse is spread out in time and the received echo of the pulse is processed with a matched filter to despread it.
- The return signal is band-limited and digitally demodulated to a complex baseband signal that, for each pulse, comprises a large number of samples.
- Each complex pair of samples (de-

noted a range gate in radar terminology) is associated with a numerical index that corresponds to a specific time offset from the beginning of the radar pulse, so that each such pair represents the energy reflected from a specific range. This energy and the average echo power are computed.

- The phase of each range bin is compared to the previous echo by complex conjugate multiplication to obtain the mean Doppler shift (and hence the mean and variance of the velocity of precipitation) of the echo at that range.

The processing for each of the four channels (see figure) requires  $>5 \times 10^9$  multiplications per second — well beyond the capabilities of traditional microprocessors. The design effort involved the application of some algorithmic tricks, careful planning of the allocation of the areas on the FPGA to the various processing functions, and exploitation of the high circuit density and performance of the commercially available FPGAs chosen for this application. The design has made it possible to perform all the processing required by the radar system on two FPGAs — each one handling the data for two of the four channels. The algorithmic tricks and other design techniques used here could be applied to FPGA implementations of other signal-processing systems in other applications in radar, general imaging, and communications.

*This work was done by Andrew Berkun and Ray Andraka of Caltech for NASA's Jet Propulsion Laboratory. Further information is contained in a TSP (see page 1). NPO-30517*





## Part 1 of a Computational Study of a Drop-Laden Mixing Layer

This first of three reports on a computational study of a drop-laden temporal mixing layer presents the results of direct numerical simulations (DNS) of well-resolved flow fields and the derivation of the large-eddy simulation (LES) equations that would govern the larger scales of a turbulent flow field. The mixing layer consisted of two counterflowing gas streams, one of which was initially laden with evaporating liquid drops. The gas phase was composed of two perfect gas species, the carrier gas and the vapor emanating from the drops, and was computed in an Eulerian reference frame, whereas each drop was tracked individually in a Lagrangian manner. The flow perturbations that were initially imposed on the layer caused mixing and eventual transition to turbulence. The DNS database obtained included transitional states for layers with various liquid mass loadings. For the DNS, the gas-phase equations were the compressible Navier-Stokes equations for conservation of momentum and additional conservation equations for total energy and species mass. These equations included source terms representing the effect of the drops on the mass, momentum, and energy of the gas phase. From the DNS equations, the expression for the irreversible entropy production (dissipation) was derived

and used to determine the dissipation due to the source terms. The LES equations were derived by spatially filtering the DNS set and the magnitudes of the terms were computed at transitional states, leading to a hierarchy of terms to guide simplification of the LES equations. It was concluded that effort should be devoted to the accurate modeling of both the subgrid-scale fluxes and the filtered source terms, which were the dominant unclosed terms appearing in the LES equations.

*This work was done by Nora A. Okong'o and Josette Bellan of Caltech for NASA's Jet Propulsion Laboratory. Further information is contained in a TSP (see page 1). NPO-30719*

## Some Improvements in Signal-Conditioning Circuits

Two documents present wide-ranging discussions of some issues in the design and operation of signal-conditioning circuits. The first document focuses on active low-pass filter circuits that contain resistors, capacitors, and operational amplifiers. It describes design and operational problems encountered previously, deficiencies of prior designs, and four design improvements to overcome the deficiencies. These improvements are as follows:

1. An offset-calibration feature in which an electronic switch isolates a filter ca-

pacitor in order to preserve its voltage during a calibration performed to measure the offset voltage of the operational amplifier;

2. Configuring a pair of complementary operational amplifiers to prevent latchup and decrease the degree of nonlinearity in overall response;
3. Minimizing distortion by taking the filter output from the operational-amplifier output nodes instead of from one of the other nodes as in prior designs; and
4. Providing for switching different feedback resistors to change filter break frequencies.

The second document addresses topics in the architecture of signal-conditioning and multiplexing circuitry. Improvements are described as being made with respect to greater compactness, increased flexibility in accommodating a variety of inputs, improvements in filter performance, simplification of wiring, and reconfigurability of designs.

*This work was done by Robert L. Shuler of Johnson Space Center. For further information, contact the Johnson Commercial Technology Office at (281) 483-3809.*

*This invention is owned by NASA, and a patent application has been filed. Inquiries concerning nonexclusive or exclusive license for its commercial development should be addressed to the Patent Counsel, Johnson Space Center, (281) 483-0837. Refer to MSC-23538/9.*







National Aeronautics and  
Space Administration